©ESO 2024

Massive stars exploding in a He-rich circumstellar medium – X.

Flash spectral features in the Type Ibn SN 2019cj and observations of SN 2018jmt

Z.-Y. Wang[1,2], A. Pastorello[3], K. Maeda[4], A. Reguitti[5,3], Y.-Z. Cai[6,7,8]★, D. Andrew Howell[9,10],
S. Benetti[3], D. Buckley[11], E. Cappellaro[3], R. Carini[12], R. Cartier[13], T.-W. Chen[14], N. Elias-Rosa[3,15],
Q.-L. Fang[4], A. Gal-Yam[16], A. Gangopadhyay[17], M. Gromadzki[18], W.-P. Gan[19], D. Hiramatsu[20,21], M.-K. Hu[22],
C. Inserra[23], C. McCully[9], M. Nicholl[24], F. Olivares E.[25], G. Pignata[26], J. Pineda-García[27], M. Pursiainen[28],
F. Ragosta[12,29], A. Rau[30], R. Roy[31], J. Sollerman[17], L. Tartaglia[32], G. Terreran[9,10], G. Valerin[3], Q. Wang[33],
S.-Q. Wang[19], D. R. Young[24], A. Aryan[14], M. Bronikowski[34], E. Concepcion[34], L. Galbany[15,35], H. Lin[6,7,8],
A. Melandri[12], T. Petrushevska[34], M. Ramirez[27,36], D.-D Shi[37,38], B. Warwick[28], J.-J. Zhang[6,7,8], B. Wang[6,7,8],
X.-F. Wang[22] ★★, and X.-J. Zhu[2,39,40]★★★

(Affiliations can be found after the references)

ABSTRACT

We present optical and near-infrared observations of two Type Ibn supernovae (SNe), SN 2018jmt and SN 2019cj. Their light curves have rise times of about 10 days, reaching an absolute peak magnitude of M_g(SN 2018jmt) = -19.07 ± 0.37 and M_V(SN 2019cj) = -18.94 ± 0.19 mag, respectively. The early-time spectra of SN 2018jmt are dominated by a blue continuum, accompanied by narrow (600−1000 km s^{-1}) He I lines with P-Cygni profile. At later epochs, the spectra become more similar to those of the prototypical SN Ibn 2006jc. At early phases, the spectra of SN 2019cj show flash ionisation emission lines of C III, N III and He II superposed on a blue continuum. These features disappear after a few days, and then the spectra of SN 2019cj evolve similarly to those of SN 2018jmt. The spectra indicate that the two SNe exploded within a He-rich circumstellar medium (CSM) lost by the progenitors a short time before the explosion. We model the light curves of the two SNe Ibn to constrain the progenitor and the explosion parameters. The ejecta masses are consistent with either that expected for a canonical SN Ib (~ 2 M$_\odot$) or those from a massive WR star ($> \sim 4$ M$_\odot$), with the kinetic energy on the order of 10^{51} erg. The lower limit on the ejecta mass ($> \sim 2$ M$_\odot$) argues against a scenario involving a relatively low-mass progenitor (e.g., $M_{ZAMS} \sim 10$ M$_\odot$). We set a conservative upper limit of ~ 0.1 M$_\odot$ for the ^{56}Ni masses in both SNe. From the light curve modelling, we determine a two-zone CSM distribution, with an inner, flat CSM component, and an outer CSM with a steeper density profile. The physical properties of SN 2018jmt and SN 2019cj are consistent with those expected from the core collapse of relatively massive, stripped-envelope (SE) stars.

Key words. circumstellar matter – supernovae: general – supernovae: individual: SN 2018jmt, SN 2019cj

1. Introduction

Supernovae (SNe) interacting with a circumstellar medium (CSM) provide an opportunity to probe the latest evolutionary stages of massive stars before their explosion. In general, the interaction of the SN ejecta with the CSM produces quite complex spectral line profiles, sometimes characterised by multiple width components, but usually dominated by a relatively narrow emission feature. The narrow emission component is thought to originate in the unshocked, photoionised CSM, which is expanding slowly (from tens to several hundreds km s^{-1}) (Dessart 2024). As a consequence, measuring the width of these narrow lines gives an indication of the velocity of the pre-SN stellar wind (e.g., Chevalier & Fransson 1994; Fransson et al. 2002; Pastorello et al. 2016; Smith 2017).

In general, interacting core-collapse (CC) SNe are divided into three observational types, depending on the identification in the spectra of individual narrow features (Gal-Yam 2017): the H-rich SNe IIn (e.g., Schlegel 1990; Filippenko 1997; Fraser 2020), the He-rich and H-poor SNe Ibn (e.g., Pastorello et al. 2007, 2008a; Hosseinzadeh et al. 2017; Maeda & Moriya 2022), and C/N/O-rich and H/He-poor SNe Icn (e.g., Fraser et al. 2021; Gal-Yam et al. 2022; Perley et al. 2022; Pellegrino et al. 2022).

The spectral properties of SNe Ibn are explained in terms of interaction between the SN ejecta and the H-deprived, He-rich CSM. The spectra of SNe Ibn are characterised by narrow He I emission lines, with full-width at half maximum (FWHM) velocities ranging from several hundred to a few thousand km s^{-1} (see e.g., Pastorello et al. 2016; Hosseinzadeh et al. 2017; Wang et al. 2021). However, in a few cases (e.g., SN 2005la, SN 2011hw, SN 2022pda; Pastorello et al. 2008b, 2015a, Cai et al., in preparation) weak H lines were observed in the spectra of some SNe Ibn, suggesting the presence of some residual H in the CSM, forming a subclass of SNe Ibn. Most SNe Ibn show relatively fast-evolving light curves, with a typical rise time of ≤ 15 days, a post-peak decline rate of $\sim 0.05−0.15$ mag day^{-1}, and a peak absolute magnitude of ≈ -19 mag (see the statistic study on SNe Ibn by Hosseinzadeh et al. 2017). However, some outliers were observed in the SN Ibn family, such as ASASSN-14ms,

---

which has a highly luminous peak at $M_V \sim -20.5$ mag (Vallely et al. 2018; Wang et al. 2021), while OGLE-2012-SN-006 and OGLE-2014-SN-131 shows an unprecedented long-lasting light curve evolution (Pastorello et al. 2015e; Karamehmetoglu et al. 2017).

Although the first discovery of this family was SN 1999cq (Matheson et al. 2000), the label 'SNe Ibn' was introduced in the study of SN 2006jc, which is considered to be the prototype of Type Ibn events (Pastorello et al. 2007). SNe Ibn are a rare group of stellar explosions, with only 66 events discovered so far[1]. Based on data from the Zwicky Transient Facility (ZTF; Bellm et al. 2019) Bright Transient Survey, Perley et al. (2020) estimated a detection rate of 0.66% for Type Ibn SNe within the ZTF transient sample. Additionally, Maeda & Moriya (2022) estimated that the observed volumetric rate of SNe Ibn is approximately 1% of all CC SNe.

Studies in the literature suggest that the progenitors of SNe Ibn can either be H-poor, massive Wolf-Rayet (WR) stars which have experienced major mass-loss events shortly before the terminal CC, or lower-mass He stars in binary systems, where the interaction with the companion favours the mass loss from the primary (e.g., Maund et al. 2016; Hosseinzadeh et al. 2019; Maeda & Moriya 2022; Wang et al. 2024b). Unfortunately, to date, there have been no direct detection of SN Ibn progenitors. Sun et al. (2020) reported the detection of a point source at the location of the SN 2006jc explosion with the Hubble Space Telescope (HST)[2], providing evidence that it is the progenitor's binary companion.

In general, SNe Ibn are observed in active star-forming regions within their host galaxies (e.g., Kuncarayakti et al. 2013; Taddia et al. 2015; Pastorello et al. 2015e). However, as a remarkable exception, PS1-12sk was detected on the outskirts of an elliptical galaxy, challenging the massive star explosion scenario for SNe Ibn (Sanders et al. 2013). Therefore, there are still many open questions regarding SNe Ibn, for example, the homogeneity of the progenitors, the origins of CSM, and the sources powering the SN light curves.

In this paper, we present our photometric and spectroscopic observational data of two Type Ibn SNe 2018jmt and 2019cj, which were observed in the framework of the extended Public European Southern Observatory (ESO) Spectroscopic Survey of Transient Objects (ePESSTO, Smartt et al. 2015). The paper is organised as follows: the information on the discovery, distance, and extinction of the two objects are reported in Section 2. In Section 3, we present the observations and the data reduction techniques. Photometric and spectroscopic analyses are presented in Sections 4 and 5, respectively. Finally, the discussion and conclusions are presented in Section 6.

2. Basic sample information

2.1. SN 2018jmt

The discovery of SN 2018jmt, attributed to the Mobile Astronomical System of the Telescope-Robots (MASTER; Lipunov et al. 2012; Gorbovskoy et al. 2013), is dated 2018 December 08.28 (epoch corresponding to MJD = 58460.28; UT dates are used throughout the paper). The object was observed in an unfiltered image, with a magnitude of 16.5 (Chasovnikov et al. 2018). However, an earlier detection was reported by the All-Sky Automated Survey for Supernovae (ASAS-SN; Shappee et al. 2014;

Kochanek et al. 2017; Jayasinghe et al. 2019) on 2018 December 05.29 (MJD = 58457.29), at a magnitude $g = 18.32 \pm 0.20$ mag[3]. The last non-detection by ASAS-SN was on 2018 December 02.31 (MJD = 58454.31) in the g-band, with an estimated limit of 18.57 mag. Soon after its discovery, the SN was classified as a Type Ibn event by the ePESSTO collaboration (Castro-Segura et al. 2018). The SN coordinates are RA = $06^h54^m47^s.100$, Dec = $-59°30'10''.80$ (J2000.0). The location of the SN within the host galaxy is shown in Fig. 1.

SN 2018jmt is possibly associated with the host galaxy PGC 370943 (2MASSJ06544633-5930163, Skrutskie et al. 2006). Due to the lack of distance information, we inferred the kinematic distance of the host galaxy from the most prominent narrow He I ($\lambda_0 = 5875.6$ Å) line in the SN spectra. We measured the central wavelength of the narrow He I lines and obtained the redshift of $z = 0.032 \pm 0.001$. Adopting a standard cosmology with $H_0 = 73 \pm 5$ km s^{-1} Mpc^{-1}, $\Omega_M = 0.27$, $\Omega_\Lambda = 0.73$ (Spergel et al. 2007), we estimated a luminosity distance $d_L = 134.7 \pm 13.6$ Mpc ($\mu = 35.65 \pm 0.22$ mag) for SN 2018jmt. Regarding the interstellar reddening, we adopt $E(B-V)_{Gal} = 0.105$ mag for the Galactic reddening contribution (Schlafly & Finkbeiner 2011), retrieved via the NASA/IPAC Extragalactic Database (NED)[4], assuming a reddening law with $R_V = 3.1$ (Cardelli et al. 1989). However, the host galaxy extinction cannot be firmly constrained due to the low signal-to-noise ratios (S/N) in our early spectra. Therefore, we adopt $E(B-V)_{Total} = 0.105$ mag as the total reddening towards SN 2018jmt.

2.2. SN 2019cj

Although the discovery of SN 2019cj was officially announced by ASAS-SN on 2019 January 03.26 (MJD = 58486.26) with a Sloan g-band brightness of 18.3 mag (AB, Nicholls & Stanek 2019), an earlier detection was obtained by the Asteroid Terrestrial-impact Last Alert System (ATLAS; Tonry et al. 2018; Smith et al. 2020; Shingles et al. 2021) survey on 2018 December 31.42 (MJD = 58483.42), with the object having an orange (o) band magnitude of $o = 19.75 \pm 0.27$ mag[5]. The last non-detection by ASAS-SN was on 2018 December 29.30 (MJD = 58481.30) in the g-band, with an estimated limit of 18.68 mag. Soon after the discovery, SN 2019cj was classified as a Type II or Type Ibn SN (Pignata et al. 2019) by ePESSTO. Its coordinates are RA = $04^h56^m22^s.977$, Dec = $-46°02'13''.68$ (J2000.0).

SN 2019cj is located 21.08" south and 1.43" east from the center of its predicted host galaxy, AM 0454-460 (PGC 130531), which is a face-on Sc-type galaxy (Loveday 1996; Moustakas et al. 2023). The location of the supernova is shown in Fig. 1. Adopting the recessional velocity of $v = 13313 \pm 49$ km s^{-1} (hence a redshift $z = 0.0444 \pm 0.0002$; Mould et al. 2000), corrected for the Virgo Cluster, the Great Attractor, and the Shapley supercluster influence, and adopting the same standard cosmological model, we obtain a luminosity distance of $d_L = 188.7 \pm 13.9$ Mpc, hence a distance modulus $\mu_L = 36.38 \pm 0.16$ mag. The Galactic reddening towards SN 2019cj is small, $E(B-V)_{Gal} = 0.016$ mag (Schlafly & Finkbeiner 2011), assuming the same R_V as for SN 2018jmt. The remote location of this SN in the outskirts of AM 0454-460, along with the low S/N in our early spectra, suggests negligible extinction from the host galaxy. For this reason, we assume the total line-of-sight red-

---

dening, $E(B-V)_{\rm tot} = 0.016$ mag, is only due to the Galactic contribution.

3. Observations and data reduction

3.1. Photometric data

We conducted multi-band optical (Sloan *griz*, Johnson-Cousins *UBV*) and near-infrared (NIR; *JHK*) follow-up campaigns of SNe 2018jmt and 2019cj starting shortly after their classification. The telescopes and instruments utilised were the following: the 3.58m New Technology Telescope (NTT) equipped with the ESO Faint Object Spectrograph and Camera 2 (EFOSC2) and the Son of Isaac (SOFI), hosted on La Silla (Chile) of the ESO. Additionally, we obtained a single epoch (2019-02-14) of SN 2018jmt photometry as part of GREAT program (Chen et al. 2018) using the Gamma-Ray Burst Optical/Near-Infrared Detector (GROND, Greiner et al. 2008), a 7-channel imager that collects multi-colour photometry simultaneously with *g'r'i'z'JHKs* bands, mounted at the 2.2m MPG telescope at ESO La Silla Observatory, Chile. Furthermore, we collected additional data through the Las Cumbres Observatory (LCO, Brown et al. 2013) global network. This network includes the 1-m class telescopes identified as fa06, fa14 and fa16, and hosted in the South African Astronomical Observatory (SAAO) in Sutherland, South Africa; the fa03 and fa15 telescopes of the Cerro Tololo Interamerican Observatory site, Chile, and the fa11 and fa12 telescopes at the Siding Spring Observatory in New South Wales, Australia.

The raw images were first pre-reduced by applying bias and overscan corrections, flat-fielding, and trimming, which are standard correction steps performed in IRAF[6] (Tody 1986, 1993). The NTT data were retrieved by the ePESSTO collaboration. The raw images from ePESSTO were pre-reduced using the dedicated PESSTO pipeline (see Smartt et al. 2015). The GROND raw images were reduced with the GROND pipeline (Krühler et al. 2008), which applies de-bias and flat-field corrections, stacks images and provides astrometry calibration. If multiple exposures were taken with the same instrument and in the same night, we combined them into stacked science frames to increase the S/N.

Subsequent photometric data reduction steps were carried out with a dedicated pipeline called *ecsnoopy*[7], which consists of several photometric packages, including DAOPHOT[8] for magnitude measurement (Stetson 1987), SEXTRACTOR[9] for source extraction (Bertin & Arnouts 1996), and HOTPANTS[10] for template subtraction (Becker 2015). The *ecsnoopy* pipeline was used for astrometric calibration, image combination, and point-spread-function (PSF) fitting photometry, with the subtraction of a reference image (referred to as the "template") when required. We directly adopted the simple PSF-fitting technique for SN 2019cj, due to its location in the outskirts of the host galaxy, while template subtraction was necessary for SN 2018jmt to remove the background contamination from the host galaxy[11]. The PSF-fitting technique consists of constructing a PSF model by selecting for each image bright and isolated stars in the SN field. The

sky background was then subtracted by fitting a low-order polynomial (e.g., a second or third order) in the SN proximity. The modelled source was subtracted from the original images, and the fitting process was repeated to minimise the residuals. When the SN was not detected, an upper limit to the object brightness was estimated.

Photometric calibration of instrumental magnitudes was performed by adopting instrumental zero points (ZPs) and color terms (CTs) inferred through observations of standard stars on photometric nights. Specifically, Johnson-Cousins filter photometry was calibrated using standard stars from the Landolt (1992) catalogue, while the Sloan data were calibrated using standards catalogued by Pan-STARRS (Chambers et al. 2016), as the fields of both SN 2018jmt and SN 2019cj were not sampled by the Sloan Digital Sky Survey (SDSS) (Abdurro'uf et al. 2022). To correct the instrumental ZPs on non-photometric nights and improve the photometric calibration accuracy, we compared the average magnitudes of local sequences of standard stars in the fields of the two SNe to those obtained on photometric nights. With the corrected ZPs, we fine-tuned the SN apparent magnitudes on all nights.

The instrumental magnitude errors were computed through artificial star experiments, in which fake stars (with a similar magnitude as the SN) were placed near the SN location. The simulated frame is then processed with the PSF fit and the magnitudes measured. The dispersion of individual artificial star experiments was combined (in quadrature) with the PSF fit and the ZP correction, providing the final errors for the photometric data.

NIR raw images required some preliminary processing procedures, such as flat-fielding, distortion corrections and the subtraction of the background contamination. To construct sky images for each filter, we median-combined several dithered science frames. We then combined sky-subtracted frames to increase the S/N. Note that these steps were performed through the PESSTO pipeline for the NTT-SOFI raw data. Seeing measurements, astrometry, PSF-fitting, and ZP corrections were carried out using *ecsnoopy* and are similar to those discussed for the optical frames. Finally, reference stars from the Two Micron All Sky Survey (2MASS[12]; Skrutskie et al. 2006) catalogue were used to calibrate the NIR instrumental magnitudes.

We also collected photometric data from the public ATLAS and ASAS-SN sky surveys for transients. The orange and cyan(*c*) band light curves were directly produced by the ATLAS data-release server [13] (Shingles et al. 2021), while some *g*-band data were obtained from the ASAS-SN Sky Patrol[14] (Hart et al. 2023). The Transiting Exoplanet Survey Satellite (*TESS*) (Ricker et al. 2015) space telescope, which is operated by the National Aeronautics and Space Administration (NASA), is equipped with four wide field-of-view optical cameras. Vallely et al. (2021) presented the early-time light curves of a sample of SNe, including SN,2018jmt, and provided a highly accurate determination of the time of explosion with negligible uncertainty. The final photometric data of SN 2018jmt and SN 2019cj are listed in Tables A.1 - A.2 in Appendix A, while their apparent light curves are shown in Fig. 2.

3.2. Spectroscopic data

Spectroscopic observations of the two SNe Ibn were carried out using the following telescopes: The 3.58m NTT equipped

---

[6] https://iraf-community.github.io/
[7] *ecsnoopy* is a package for SN photometry using PSF fitting and/or template subtraction developed by E. Cappellaro. A package description can be found at http://sngroup.oapd.inaf.it/snoopy.html.
[8] http://www.star.bris.ac.uk/~mbt/daophot/
[9] www.astromatic.net/software/sextractor/
[10] https://github.com/acbecker/hotpants/
[11] The *UBVgri* template images were taken through LCO-fa15 in November 2023, i.e. about 5 years after the discovery.

[12] http://irsa.ipac.caltech.edu/Missions/2mass.html/
[13] https://fallingstar-data.com/forcedphot/
[14] https://asas-sn.osu.edu
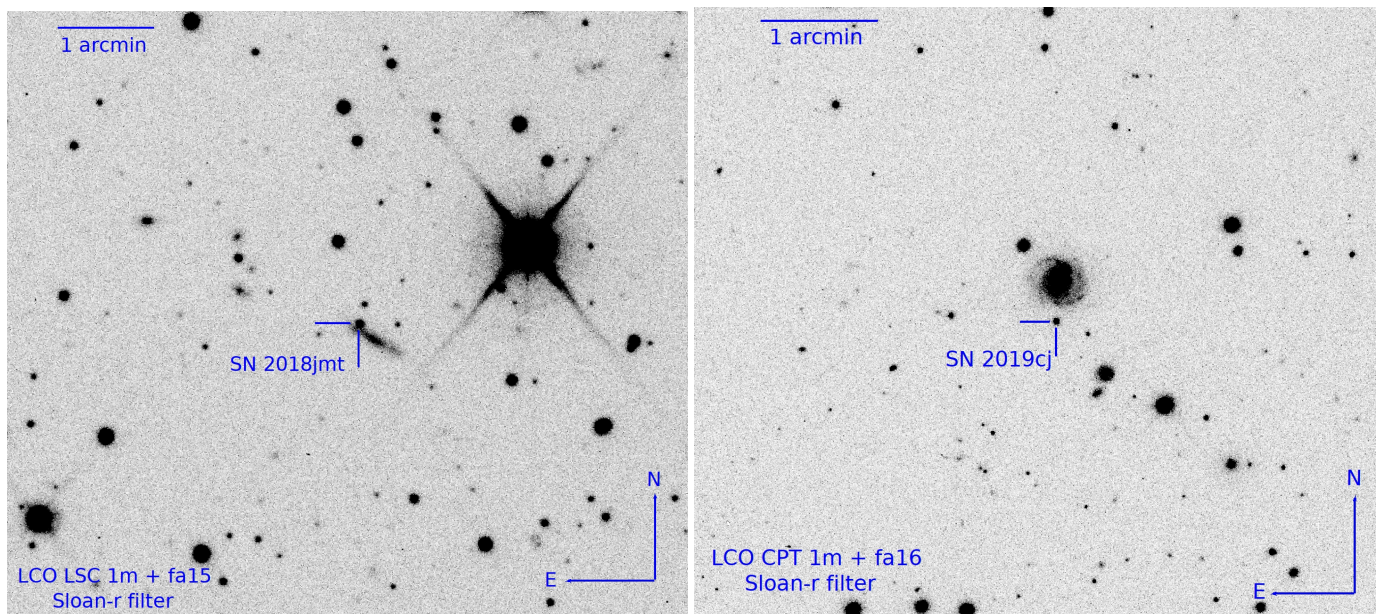
Fig. 1. Images of the locations of SN 2018jmt and SN 2019cj, taken on 2018 December 20 and 2019 January 11, respectively, by the LCO telescopes with the *r*-filter. The orientation and scale of the images are reported.

with EFOSC2; the 4.1m Southern Astrophysical Research Telescope (SOAR) at Cerro Pachón, Chile, equipped with the Goodman High Throughput Spectrograph (GHTS); the 11m Southern African Large Telescope (SALT) at the SAAO equipped with the Robert Stobie Spectrograph (RSS); the 2m Faulkes telescope with the FLOYDS spectrograph, hosted by the Siding Spring Observatory, which is also part of the LCO global network.

All raw spectral data were reduced following the standard steps in IRAF[15] (Tody 1986, 1993) or with dedicated pipelines such as PySALT[16] (Crawford et al. 2010), PESSTO (Smartt et al. 2015) and FLOYDS[17]. The pre-reduction steps, such as bias, overscan, flat-fielding correction, and trimming, are similar to those described for the imaging data. Then, the one-dimensional (1D) spectra were optimally extracted from the 2D images. Wavelength calibrations were performed using arc lamps, while flux calibrations were performed using spectrophotometric standard stars taken on the same nights. Subsequently, the strongest telluric absorption bands, such as O_2 and H_2O, were removed from the SN spectra using the spectra of the standard stars. Finally, the accuracy of flux calibration for all spectra was checked against the coeval photometric data. The information on the instrumentation used for the spectroscopic observations is reported in Tables B.1 and B.2 (Appendix B).

4. Photometry

4.1. Apparent light curves

We conducted a continuous monitoring of the photometric evolution of SN 2018jmt and SN 2019cj for about three months after discovery. The optical and near-infrared light curves of SNe 2018jmt and 2019cj are shown in Fig. 2.

The determination of the explosion epoch of a SN is located between the last non-detection and the first detection of the event. Vallely et al. (2021) reports a relatively accurate explosion

Table 1. Decline rates of the light curves of SN 2018jmt and SN 2019cj.

	SN 2018jmt		
Filter	$\gamma^{\ddagger}_{0-15}$	$\gamma^{\ddagger}_{15-60}$	$\gamma^{\ddagger}_{60-100}$
U	17.37±0.57	3.32±1.12	-
B	15.43±1.14	4.17±0.21	-
g	14.02±1.54	4.09±0.15	-
V	11.10±0.38	4.61±0.14	-
r	12.93±0.83	4.21±0.24	-
i	9.72±0.75	6.00±0.39	-
J	-	7.59±0.66	2.74±1.35
H	-	4.88±1.30	2.22±2.30
K	-	5.74±0.99	-0.95±2.36
	SN 2019cj		
Filter	$\gamma^{\ddagger}_{0-15}$	$\gamma^{\ddagger}_{15-48}$	$\gamma^{\ddagger}_{48-80}$
U	10.84±0.67	14.62±0.88	-
B	8.68±0.58	13.53±0.78	-
g	7.33±0.43	11.78±0.78	-
V	7.08±0.50	10.97±0.22	-
r	4.99±0.34	9.19±0.41	-
i	3.46±0.30	8.93±0.30	-
z	2.46±0.46	-	-
o	5.11±9.27	-	-
J	1.61±2.80	5.06±0.36	6.51±0.83
H	-1.45±2.99	2.89±0.34	5.23±0.72
K	-8.54±4.46	1.82±0.46	3.56±0.72

‡ in mag $(100 \text{ d})^{-1}$

time of 58455.01 ± 0.24 in the *TESS T*-band for SN 2018jmt, based on a curved power-law fit to the pre-peak TESS light curve. For SN 2019cj, the last non-detection t_l dates back to MJD = 58479.4 (in the ATLAS *o* band), whilst the first detection epoch t_d is MJD = 58483.4 (in the *o* band). The midpoint between t_l and t_d provides a rough estimate of the explosion epoch. The maximum error is given by half of the difference between t_l and t_d. Using this method, we obtain the explosion epoch of

---

[15] http://iraf.noao.edu/
[16] http://pysalt.salt.ac.za/
[17] https://lco.global/documentation/data/floyds-pipeline/
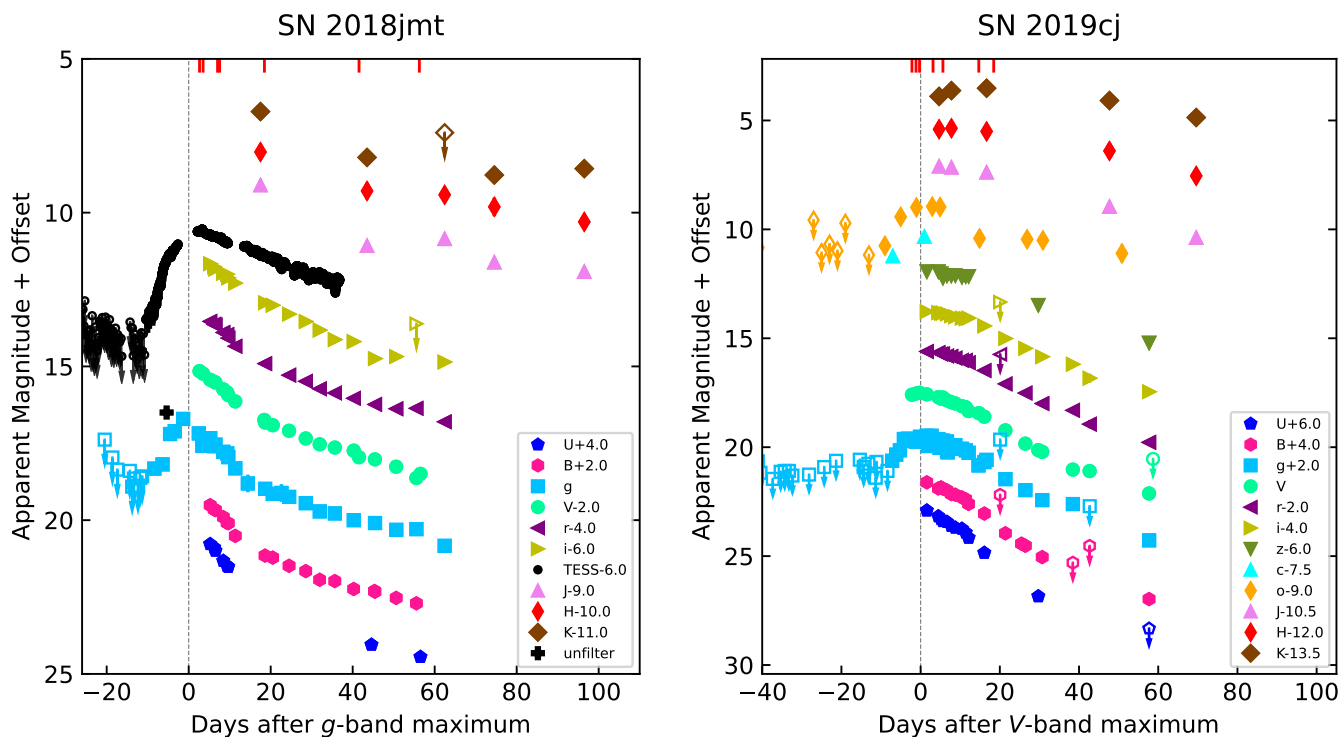
Fig. 2. Multi-band light curves of SN 2018jmt (left) and SN 2019cj (right). A dashed vertical line is used to visually represent the reference epoch, which corresponds to the g/V-band maximum light. The epochs of our spectra are marked with vertical solid red lines on the top. The upper limits are indicated by empty symbols with down-arrows. For clarity, the light curves are shifted by constant amounts reported in the legends. In most cases, the errors associated with the magnitudes are smaller than the plotted symbol sizes.
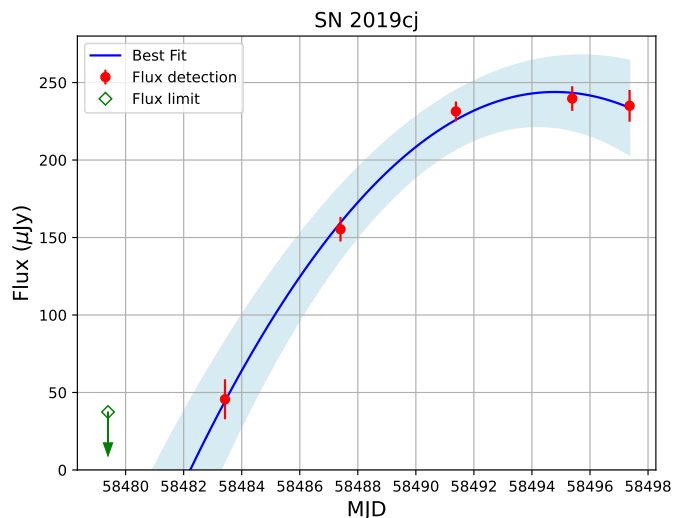
Fig. 3. Estimate of the explosion epoch for SN 2019cj. The ATLAS-o light curves of SN 2019cj (detections use red dot markers, limits use green diamond markers) are shown in flux space (expressed in μJy). The early light curves are fitted with a 2nd-order polynomial, represented by a blue solid line. The blue shaded region around the fitted curve represents the 3-σ uncertainty in the fitting process.

MJD = 58481.4±2.0 for SN 2019cj. To improve our estimate of the explosion epoch of SN 2019cj, we adopted the fireball expansion method. As shown in Fig. 3, we applied a second-order polynomial fit to the data captured within a 20-day period before and around the peak of the light curve in flux space (e.g., González-Gaitán et al. 2015). Following this approach, we estimated the explosion epoch, as the time when the flux reaches 0,

to be MJD = 58482.2 ± 1.1 for SN 2019cj, which will be adopted hereafter.

To estimate the peak magnitude of SN 2018jmt, a 3rd-order polynomial fit is performed on the g-band light curve data within a 4-week period centred around the peak in magnitude space. We obtained a peak magnitude of g = 17.0 ± 0.3 on MJD = 58465.7 ± 1.2 for SN 2018jmt. Using a similar approach, we estimated the peak magnitude of SN 2019cj as 17.5 ± 0.1 on MJD = 58492.4 ± 0.2 in the V-band.

We also estimated the post-maximum decline rate of SN 2018jmt and SN 2019cj in various bands by performing a linear regression on the post-peak data. The results are reported in Table 1. Given the observed change in the slope of the light curves of SN 2018jmt at approximately +15 d in the optical and +60 d in the NIR, we computed the decline rates in three different time intervals. We observe a notable difference in the decline rates among different filters. Specifically, the bluer light curves exhibit a faster decline compared to the redder ones. This trend is particularly evident during the early decline phase (γ_{0-15} in Table 1).

From 0 to 15 days, the light curves of SN 2019cj show a faster decline in the blue bands, while in the NIR, the object is still rising towards its peak. Later on, at phases beyond 15 days, the light curves show a steeper decline (e.g., γ_{15-48}(B) ≈ 0.14 mag d^{-1}, γ_{15-48}(r) ≈ 0.09 mag d^{-1}, γ_{15-48}(K) ≈ 0.02 mag d^{-1}). An increased rate of decline in the optical luminosity at late phases is frequently observed in SNe Ibn (e.g., Mattila et al. 2008; Pastorello et al. 2015c, see also other examples in Section 4.3).
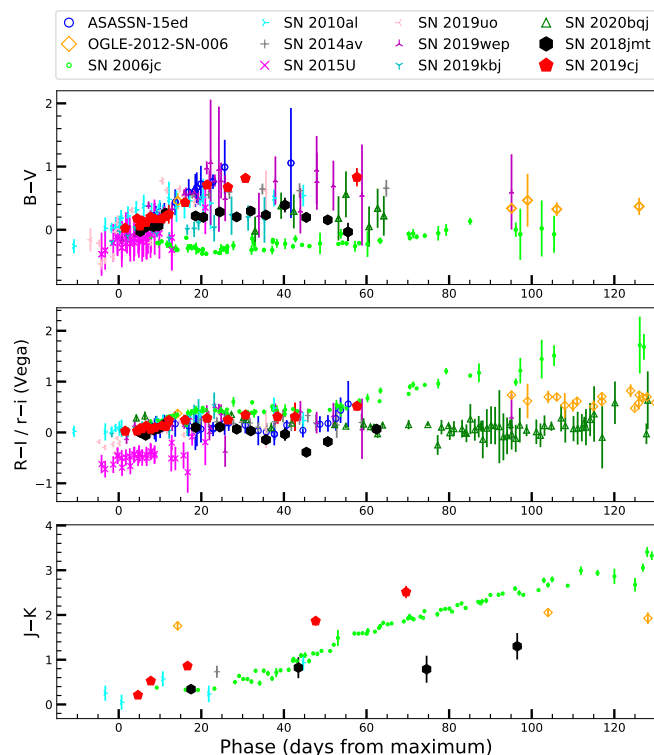
Fig. 4. Colour evolution of SN 2018jmt and SN 2019cj, compared with those of a sample of SNe Ibn. Top panel: $B - V$ colour curves; Middle panel: $R - I / r - i$ colour curves; Bottom panel: $J - K$ colour curves. The colour curves are corrected for Galactic and host galaxy extinction.

4.2. Colour evolution

Figure 4 displays the colour evolution of SN 2018jmt and SN 2019cj, along with those of other well-studied SNe Ibn, including ASASSN-15ed (Pastorello et al. 2015c), OGLE-2012-SN-006 (Pastorello et al. 2015e), SN 2006jc (Pastorello et al. 2007), SN 2010al (Pastorello et al. 2015a), SN 2014av (Pastorello et al. 2016), SN 2015U (Pastorello et al. 2015d; Shivvers et al. 2016), SN 2019uo (Gangopadhyay et al. 2020), SN 2019wep (Gangopadhyay et al. 2022), SN 2019kbj (Ben-Ami et al. 2023), and SN 2020bqj (Kool et al. 2021).

At an early stage, ~5 days from maximum, SN 2018jmt exhibits intrinsic $B - V$ and $r - i$ colours that are both close to 0 mag. At around +10 days, the object undergoes a transition towards red colours, with $B - V \sim 0.3$ mag and $r - i \sim 0.1$ mag. This is followed by a period, from +10 to +40 days, during which the $B - V$ colour is slowly increasing to 0.4 mag, while the $r - i$ colour is nearly constant. Later on, the colours of SN 2018jmt become bluer again. Similarly, the $r - i$ colour reaches its minimum value of approximately −0.4 mag at around +45 days. After that, the $r - i$ colour starts to rise again to +0.1 mag at +62 days. The $B - V$ colour behaviour of SN 2019wep, SN 2015U, and SN 2019uo is similar to that of SN 2018jmt, becoming initially redder and then turning bluer again. The $R - I / r - i$ colour behaviour of SN 2010al, SN 2019kbj, and SN 2014av, like SN 2018jmt, shows a trend towards redder in the early stages, followed by a transition to bluer. The $J - K$ colour evolution follows a similar trend as the $B - V$ and $r - i$ ones, becoming gradually redder from 0.3 mag to 1.3 mag up to 100 days, like SN 2010al.

For SN 2019cj, the $B - V$ colour evolves steadily from approximately 0 mag near the maximum to ≈0.8 mag at around
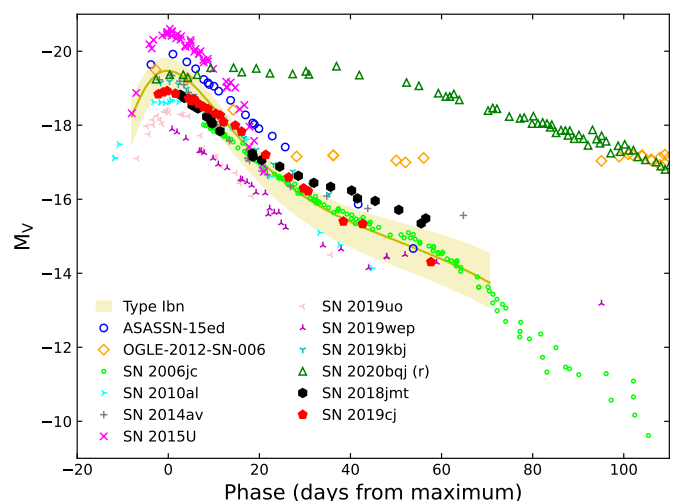
Fig. 5. Absolute V-band light curve of SN 2018jmt and SN 2019cj compared to other SNe Ibn and the SN Ibn template presented by Hosseinzadeh et al. (2017).

+30 days (as shown in Fig. 4). Beyond 30 days, the $B - V$ colour remains fairly constant. The evolution trend of $B - V$ colour is similar to ASASSN-15ed, SN 2010al and SN 2014av. Similarly, from the maximum to about 1 month after peak, the $r - i$ colour increases from approximately 0 mag to 0.3 mag. Between 30 and 45 days, also the $r - i$ colour remains constant, although - at around 60 days - $r - i$ rises again towards redder colours (0.5 mag). The evolution trend of $R - I / r - i$ colour is similar to that of SNe 2015U, 2019uo, and OGLE-2012-SN-006, although the timescales can be significantly different among individual SNe. In contrast to the optical colours, the $J - K$ colour rises monotonically from 0.2 to 2.5 mag over the entire 2 months of follow-up, like SN 2006jc.

4.3. Absolute light curves

Taking into account the distance and reddening estimates reported in Section 2, we calculate for SN 2018jmt the absolute magnitude at maximum to be $M_g = -19.03 \pm 0.37$ mag, while the V-band peak absolute magnitude of SN 2019cj is $M_V = -18.94 \pm 0.19$ mag. A comparison of the absolute V-band magnitudes for a subset of the Type Ibn SN sample is presented in Fig. 5. When V-band observations were not available, we included observations in adjacent bands for the comparison. For example, in the case of SN 2020bqj, we utilised observations in the r-band. Upon comparing the V-band light curves of SN 2018jmt and SN 2019cj with those of other Type Ibn SNe, we find that they generally follow the behaviour of the template presented by Hosseinzadeh et al. (2017) around the maximum light. SNe Ibn are relatively luminous, with most of them having absolute V-band magnitudes around −19 mag, but all falling within the range of −18 mag to −21 mag.

The heterogeneity of SNe Ibn is more evident in the post-peak decline, as many objects display an almost linear post-peak optical drop, while a few others may show a light curve with double-phase declines: an initially faster luminosity drop followed by a much slower decline. The most extreme case is OGLE-2012-SN-006, which experienced an early decline slope of ≈ 8 mag $(100 \, \mathrm{d})^{-1}$, followed by an extended phase characterised by a nearly flat light curve (~0.1 mag $(100 \, \mathrm{d})^{-1}$ between 25 and 130 days, and 2 mag $(100 \, \mathrm{d})^{-1}$ thereafter). Another ex-
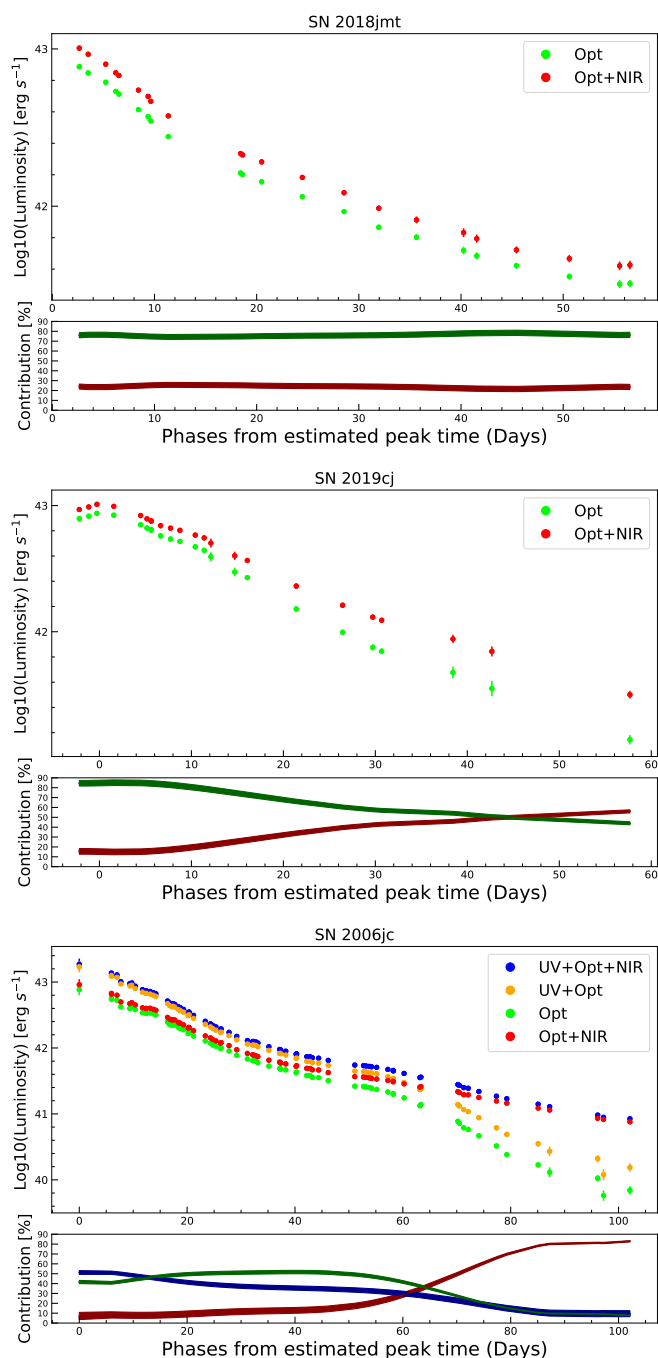
Fig. 6. Top panels: Pseudo-bolometric light curves of SNe 2018jmt, 2019cj and 2006jc, along with the light curves constructed using the UV + optical, just optical, and optical + NIR photometry. Bottom panels: Evolution of the contribution of the individual electromagnetic regions with time computed as a percentage of the pseudo-bolometric luminosity. In the comparison, we adopted the following colour codes: UV = dark blue, Optical = dark green, and NIR = dark red.

ample is SN 2020bqj, which exhibits a plateau between −19.1 and −19.3 mag in the *r*-band that persists for 40 days, followed by a linear decline lasting over 90 days at a rate of 4 mag (100 d)$^{-1}$.

4.4. Pseudo-bolometric light curves

We calculated the "optical" pseudo-bolometric light curves of SNe 2018jmt and 2019cj by integrating the flux contributions from individual optical bands. In our analysis, we made the assumption that the flux outside the integration limits is zero. When photometric data were not available for certain epochs in a particular filter, we estimated the flux contribution from the missing bands by interpolating between epochs with available data or extrapolating from earlier or later available epochs, assuming a consistent colour evolution. We also computed pseudo-bolometric light curves, including the contribution of ultraviolet (UV) and NIR photometry when available. The pseudo-bolometric light curves for SN 2018jmt, SN 2019cj, and the prototypical SN 2006jc are displayed in the top panels of Fig. 6. The relative flux contribution of each electromagnetic domain to the overall pseudo-bolometric light curve is shown in the lower panels of Fig. 6.

Public *TESS* data of SN 2018jmt would potentially help tracking the evolution of its bolometric luminosity in the pre-maximum phase. However, the information on the colour or spectroscopic evolution at those early phases is not available. Besides, there are known issues regarding the photometric calibration across multiple sectors for *TESS* (Vallely et al. 2021). In Vallely et al. (2021), a method was employed where the flux offset was selected to match the linear extrapolations from the last ∼ 2 days of the earlier sector and the first ∼ 2 days of the later sector for flux calibration across different sectors. In the case of SN 2018jmt, this approach may introduce a significant bias when comparing flux, and thus a photometric correction, between pre- and post-maximum phases because the peak lies in the sector gap. As a result, linear extrapolation can be a poor approximation for the light curve in the gap. Because of these two factors, there would be major uncertainties on the bolometric correction to apply. For this reason, we only use traditional broad-band observations to compute a pseudo-bolometric light curve for SN 2018jmt.

The lack of UV observations for SNe 2018jmt and 2019cj limits our ability to accurately determine the real bolometric luminosity at peak, when the UV contribution is expected to be significant. Therefore, we can only provide a lower limit to the maximum luminosity for the two objects, i.e., $L > 1.01 \times 10^{43}$ erg s^{-1}. Throughout the evolution of SN 2018jmt , only minor changes are registered in the relative contribution of the optical and NIR luminosity. The flux contribution of the optical bands dominates the bolometric luminosity, as it accounts for approximately 76% of the overall emission. We note, however, that during phases later than +60 days, the object fades below the detection thresholds in the optical, while it remains visible in the NIR domain up to 100 days. The NIR light curves also show an evident flattening, suggesting a dramatic increase in the luminosity contribution of the NIR bands over the optical ones.

It is worth noting that the contribution from near-infrared (NIR) emission to the pseudo-bolometric light curve of SN 2019cj is relatively small around the time of maximum brightness, as it accounts for ∼ 15% of the total luminosity. However, as time progresses, the NIR contribution becomes progressively larger. Interestingly, a similar behaviour was also observed in SN 2006jc, where the NIR contribution increased with time and became more dominant at later phases (bottom panel of Fig. 6), and was attributed to the contribution to warm dust in a cool dense shell (Mattila et al. 2008; Smith et al. 2008). Unfortunately, we were not able to obtain photometry data for SNe 2018jmt and 2019cj beyond 60 days after their discovery.
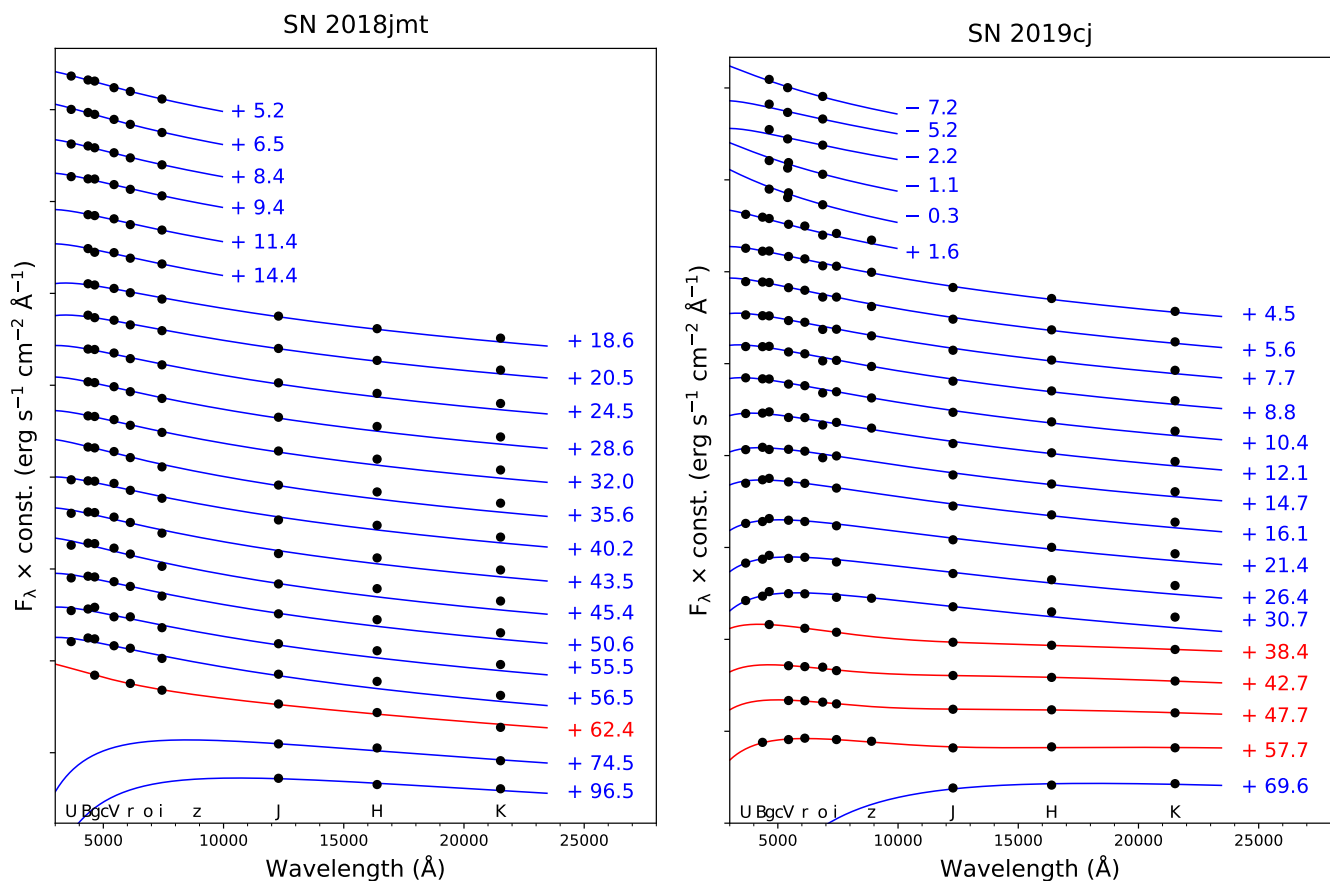
Fig. 7. SED evolution of SNe 2018jmt (left panel) and 2019cj (right panel). The lines represent the best fitted blackbody functions, which are overplotted on each SED. Blue lines are the best fits of the single blackbody, while red lines are the best fits of the two-component blackbodies. Epochs reported to the right of each SED are relative to their maximum light. SEDs have been shifted vertically by an arbitrary constant for clarity.

4.5. Spectral energy distribution (SED) analysis

In order to compare in a meaningful way SN 2018jmt, SN 2019cj and the prototypical Type Ibn SN 2006jc, we constructed their pseudo-bolometric light curves based on the observed wavelength range (see details in Section 4.4). Instead, to better estimate the full bolometric light curves of SNe 2018jmt and 2019cj, we fitted the broad-band photometry with a blackbody curve, extrapolating the luminosity contribution of the blackbody tails outside the observed range. To do so, we performed blackbody fits on the spectral energy distributions (SEDs) of SN 2018jmt and SN 2019cj at different epochs, following the descriptions in Cai et al. (2018). The resulting full bolometric light curves are used to model SNe 2018jmt and 2019cj, as presented in Section 4.7.

In Fig. 7, we show the SED evolution of SNe 2018jmt and 2019cj with their best blackbody fits. During the early and middle phases of evolution, the SEDs of both SNe 2018jmt and 2019cj are well-fitted by a single blackbody. At late-time epochs, a single blackbody is unable to well reproduce the NIR fluxes and hence a second blackbody component is needed. The optical domain is represented by a "hot" blackbody associated to the SN photosphere, in contrast with the "warm" blackbody which emerges at late phases. Specifically, as shown in the left panel of Fig. 7, the SEDs of SN 2018jmt are well-fitted by a single blackbody until epoch +56.5 d. At the epoch +62.4 d, the SED clearly reveals a NIR flux excess over a single blackbody model, hence it was fitted with two-component (hot+warm components) blackbody functions. Although the NIR flux excess is likely at-

tributed to the newly formed dust, there is also a relevant contribution from the emission lines in the SN spectra, which can bring deviations from a thermal continuum (see the late spectra of SN 2018jmt in the top panel of Fig. 11).

The onset of dust formation in SN 2006jc, starting at ~55 d past maximum, is marked by a sharp decline in the optical light curves, coincidental with a relative increase in the NIR fluxes (see e.g., Di Carlo et al. 2008; Mattila et al. 2008; Anupama et al. 2009). Unfortunately, since the lack of simultaneous observations in optical bands at late epochs from +62.4 to +96.5 d, our limited NIR observations cannot give us a stringent constraint on the possible dust formation for SN 2018jmt. Assuming the late-time NIR emission is purely due to dust condensation, it is possible to obtain an estimate of the dust mass for SN 2018jmt using the methods adopted and described in Fox et al. (2011); Gan et al. (2021); Wang et al. (2024a). We adopt the species of dust grains made of graphite and silicate with the same size distribution ($a = 0.1 \ \mu$m). The inferred dust masses are about $3 \times 10^{-6} \ M_\odot$ (graphite dust) and $3 \times 10^{-5} \ M_\odot$ (silicate dust), respectively. It is important to note that these values have to be considered as upper limits, due to our simplifying assumptions on dust formation. The SED evolution of SN 2019cj is similar to that observed in SN 2018jmt (see the right panel of Fig. 7), we hence adopted the same approach and estimated upper limits on the dust masses in SN 2019cj of the order of several $10^{-4} \ M_\odot$ for both dust species.
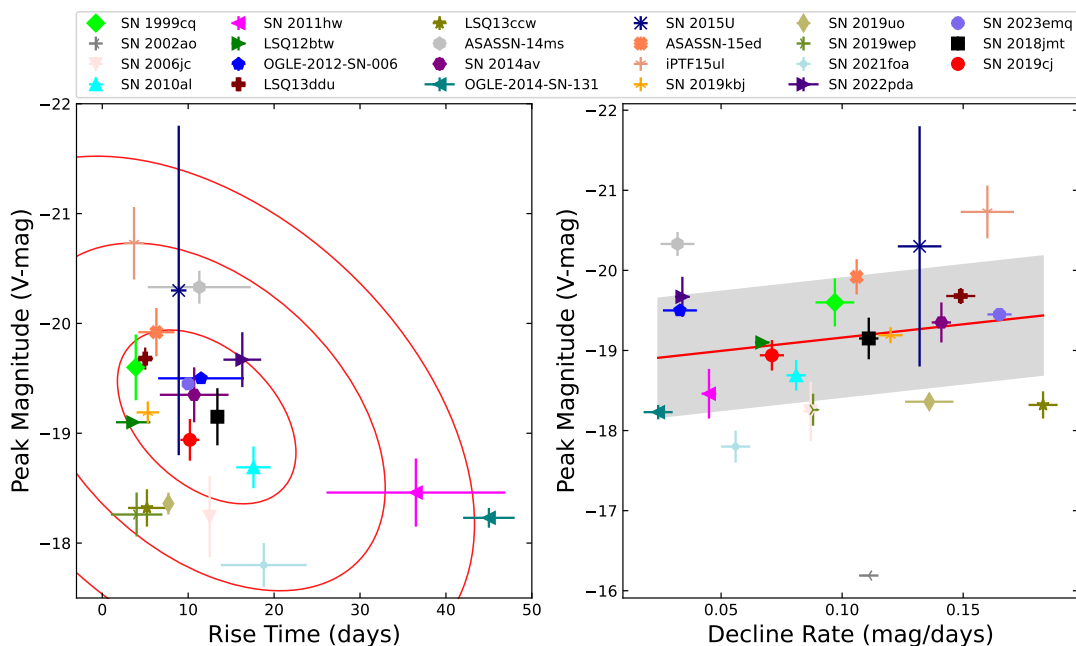
Fig. 8. Phase-space diagrams showing peak magnitudes vs. rise time (left), and peak magnitudes vs. decline rates (right) for a sample of SNe Ibn, including SNe 2018jmt and 2019cj. In the left panel, three red ellipses represent the 1σ, 2σ, and 3σ confidence intervals, indicating regions where approximately 68.27%, 95.45%, and 99.73% of the points are expected to lie, respectively. These ellipses are centered at the mean values of the points and are oriented according to the principal components of the covariance matrix. In the right panel, linear fitting was applied to the observed data, and the 95% confidence interval was calculated using a standard deviation multiplier of 1.96 to determine the shaded region. Data for comparison objects are taken from Matheson et al. (2000); Pastorello et al. (2007, 2008b); Mattila et al. (2008); Pastorello et al. (2008a); Sanders et al. (2013); Morokuma et al. (2014); Gorbikov et al. (2014); Pastorello et al. (2015d,b,e,a,c, 2016); Karamehmetoglu et al. (2017); Hosseinzadeh et al. (2017); Vallely et al. (2018); Wang & Li (2020); Clark et al. (2020); Gangopadhyay et al. (2020); Prentice et al. (2020); Karamehmetoglu et al. (2021); Kool et al. (2021); Gangopadhyay et al. (2022); Reguitti et al. (2022); Pursiainen et al. (2023); Ben-Ami et al. (2023); Wang et al. (2024b); Cai et al., in preparation.

4.6. Observational parameter correlations

To better characterise the light curve evolution of SN 2018jmt and SN 2019cj in the context of SN Ibn variety, we present in Fig. 8 the locations of a large Type Ibn SN sample in the diagrams of absolute peak magnitude versus rise time, and absolute peak magnitude versus decline rate. Note that the rise time in the V-band for SN 2018jmt was actually estimated using the g-band. Furthermore, the V-band absolute peak magnitude was extrapolated based on the initial decline rate observed in the V-band. All of this adds uncertainty to the estimates for this object.

The two objects fall in the 1σ confidence interval in the left panel, and their rise times and peak magnitudes are comparable to the median values observed in the Type Ibn SN sample (median rise time = 9.6 days, median peak magnitude = −19.19 mag). In the right panel, both SN 2018jmt and SN 2019cj fall within the 95% confidence interval (shaded area). SN 2018jmt and SN 2019cj exhibit characteristics similar to other SNe Ibn in our sample, suggesting that they adhere to the typical characteristics of Type Ibn SNe and likely share a similar origin.

4.7. Light curve modelling

In this section, we present the bolometric light curve modelling of SNe 2018jmt and 2019cj, adopting the (1D spherical) model framework of Maeda & Moriya (2022), under the assumption that their optical emissions are entirely powered by the SN-CSM interaction. We assume a broken power law for the density structure of the SN ejecta, with the outer power slope fixed to be $n = 7$ ($\rho_{\rm ej} \propto v^{n}$), while the inner part is represented by a flat distri-

bution. This setup allows the ejecta mass ($M_{\rm ej}$) and the kinetic energy of the expansion ($E_{\rm K}$), used as the input parameters, to determine the properties of the SN ejecta. The CSM density distribution is given as $\rho_{\rm CSM}(r) = 10^{-14}D'(r/5\times10^{14}~{\rm cm})^{-s}~{\rm g~cm^{-3}}$, specified by the parameters D' and s, if a single power-law is assumed.

Fig. 9 shows the results of the light curve models, and Fig. 10 shows the derived CSM density distribution. These models assume $M_{\rm ej} = 2~M_{\odot}$, and the $E_{\rm K}$ required to fit the light curve is derived to be 1.6 and 1.9×10^{51} ergs, for SNe 2018jmt and 2019cj, respectively. We introduced a two-component CSM for both SNe (see below), represented by the inner and outer components having different sets of CSM parameters. For the outer components, $(s, D') = (2.6 \pm 0.1, 4.2 \pm 0.3)$ for SN 2018jmt, and $(2.8 \pm 0.1, 4.4 \pm 0.3)$ for SN 2019cj; for the inner components, $(s, D') = (0.0 \pm 0.5, 1.0 \pm 0.3)$ for SN 2018jmt, and $(0.1 \pm 0.5, 0.8 \pm 0.2)$ for SN 2019cj. The uncertainties here only account for the errors in the bolometric luminosities and the distances; these errors should be treated as lower limits, since the systematic uncertainties linked to the assumptions in the emission model are difficult to quantify and are not included here. The relative errors both in s and D' are larger for the inner components, reflecting the larger errors in the BB fits in the pre-peak epochs. Overall, the inferred physical properties are within the range derived for a sample of SNe Ibn (Maeda & Moriya 2022), both for the SN ejecta and CSM. This is expected since the observational properties of the two SNe are similar to other SNe Ibn. Note that the CSM densities of SNe 2018jmt and 2019cj are on the highest side of the SNe Ibn analyzed by Maeda &
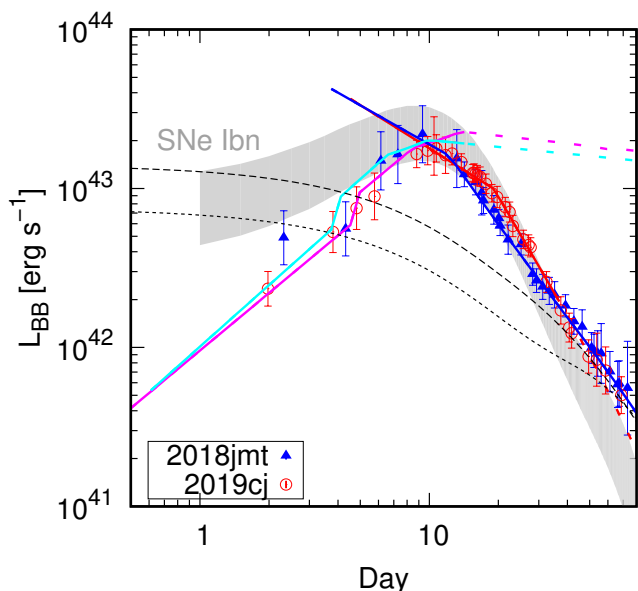
Fig. 9. Models for the bolometric light curves of SNe 2018jmt (blue triangles) and 2019cj (red circles). The models shown here assume M_{ej} = $2M_\odot$, resulting in E_K = 1.6 and 1.9×10^{51} ergs for SNe 2018jmt and 2019cj, respectively. The CSM parameters are as follows; for the outer components: $(s, D') = (2.6, 4.2)$ for SN 2018jmt (blue), and $(2.8, 4.4)$ for SN 2019cj (red); for the inner components: $(s, D') = (0.0, 1.0)$ for SN 2018jmt (cyan), and $(0.1, 0.8)$ for SN 2019cj (magenta). The thick-dashed curve is the expected contribution from the ^{56}Ni/Co decay with $M(^{56}$Ni$) = 0.15M_\odot$ taking into account the optical depth to the decay γ-rays adopting $M_{ej} = 2M_\odot$ and $E_K = 1.6 \times 10^{51}$ erg (for SN 2018jmt), which sets the upper limit for $M(^{56}$Ni$)$. The same curve but with $M(^{56}$Ni$) = 0.08M_\odot$ is shown by the thin-dashed line, for the case adopting $M_{ej} = 4M_\odot$ and $E_K = 2.3 \times 10^{51}$ erg.

Moriya (2022), but it can partly be an artifact; they used quasi-bolometric LCs and therefore might underestimate the CSM densities for the samples of SNe Ibn shown here.

As discussed by Maeda & Moriya (2022), the parameters of the CSM (s and D') can be well constrained from the post-peak light curves. The ejecta properties are on the other hand not uniquely determined. In the post-peak light curves (i.e., after the shock enters into the outer CSM component), the kink where the decline rate accelerates can be interpreted as a transition phase of the shock from the cooling regime to the adiabatic regime, and E_K is determined from this transition for a given M_{ej}. However, the outer ejecta structure degenerates in terms of a combination of M_{ej} and E_K, and for $n = 7$ adopted here, this scaling is given as $E_K \propto \sqrt{M_{ej}}$ (e.g., Moriya et al. 2013). Models with more massive ejecta can reproduce essentially the same light curve if the ejecta properties follow this relation; for example, the light curves of SNe 2018jmt and2019cj can be fit with M_{ej} = 4 $M_\odot$ if E_K is increased to ~ $(2.3 - 2.7) \times 10^{51}$ erg. The same applies to the less-massive ejecta case, but with another constraint: the ejecta mass cannot be too low, otherwise the reverse shock reaches the inner part of the ejecta too early (which is the argument used by Nagao et al. 2023 in constraining the ejecta properties for SNe Icn). From the light curve calculations, we find the lower limits for the ejecta masses as $M_{ej} > 1.6 M_\odot$ for SN 2018jmt and $> 1.8 M_\odot$ for SN 2019cj.

Under the model framework, the CSM density distribution is uniquely determined. Similar CSM density structures are derived for SNe 2018jmt and 2019cj, both within the range found for a sample of SNe Ibn. The slopes of the outer components are

similar to other SNe Ibn ($s \sim 2.5 - 3$; Maeda & Moriya 2022), indicating the increase of the mass-loss rate in the last few years toward the explosion. With the (outer) CSM parameters used to fit their post-peak light curves, we find that the diffusion time scale becomes too short (a few days) compared to the rise time (about 10 days). This indicates that the inner part of the CSM density distribution could deviate from the extrapolation from the outer part of the CSM distribution. We are thus motivated to introduce the inner CSM component separately from the outer component. By adopting the flatter density distribution for the inner part (Fig. 10), the pre-peak light curve evolution is well reproduced (Fig. 9).

The two-component CSM, with the flat part inside and the steep part outside, has been inferred for a few SNe Ibn following a similar analysis (Maeda & Moriya 2022). We note that this may likely be a common property of SNe Ibn; this analysis requires intensive photometric data in the pre-peak phase, and the flat inner part has been frequently inferred when such data are available. This highlights the importance of discovering SNe Ibn soon after the explosion and coordinating the high-cadence and intensive follow-up observations immediately after the discovery, as demonstrated in the present work for SNe 2018jmt and 2019cj.

Most of the SNe Ibn decline rapidly after the peak without requiring an additional energy input from the ^{56}Co decay; this sets the upper limits for the masses of ^{56}Ni ejected in SNe Ibn, which have been found to be lower than the typical amount estimated for canonical SNe Ib/Ic (Drout et al. 2011; Lyman et al. 2016; Ouchi et al. 2021; Maeda & Moriya 2022). We performed this test in Fig. 9, where the two light curves powered by the hypothetical ^{56}Ni/^{56}Co decay for the cases with M_{ej} = 2 and 4 $M_\odot$ for SN 2018jmt are shown. Similar limits are obtained for SN 2019cj. The upper limits thus obtained, $M(^{56}$Ni$)$ = 0.15 or 0.08 $M_\odot$, are below the mean ^{56}Ni production found in a sample of canonical SNe Ib/c (Meza & Anderson 2020, but see Ouchi et al. 2021). However, the limits here are not very strong and within the diversity of canonical SNe Ib/c; longer-term follow-up observations until later epochs might have placed a stronger constraint, as were found for some SNe Ibn.

5. Spectroscopy

5.1. Spectral sequence of SN 2018jmt

SN 2018jmt was monitored in optical spectroscopy from its discovery until approximately 60 days after maximum brightness. Top panel of Fig. 11 displays, in chronological order, our spectra of SN 2018jmt. The first spectrum shown corresponds to the classification spectrum (Castro-Segura et al. 2018). During the entire observational period, the spectra exhibit a modest evolution. The He I lines are the most prominent features observed in the spectra of SN 2018jmt. Some of these lines exhibit complex profiles, with narrow features overlaid on broader line components (e.g. in the +18 d spectrum).

The earlier spectra of SN 2018jmt reveal a blue continuum. By fitting a blackbody model to the first four spectra (taken at 2.6, 3.5, 7.0, and 7.5 days after the maximum light), the photospheric temperature ranges from 12,000 to 9,000 K. Notably, significant P-Cygni profiles are observed in the He I 5876 Å line, with the minimum being blueshifted by about 600 - 1000 km s^{-1}. Several He I lines are also identified at 4471, 4921, 5016, 6678, 7065, and 7281 Å.

Furthermore, we note the presence of a weak and narrow Hα with a P-Cygni profile (the minimum of the P-Cygni absorption
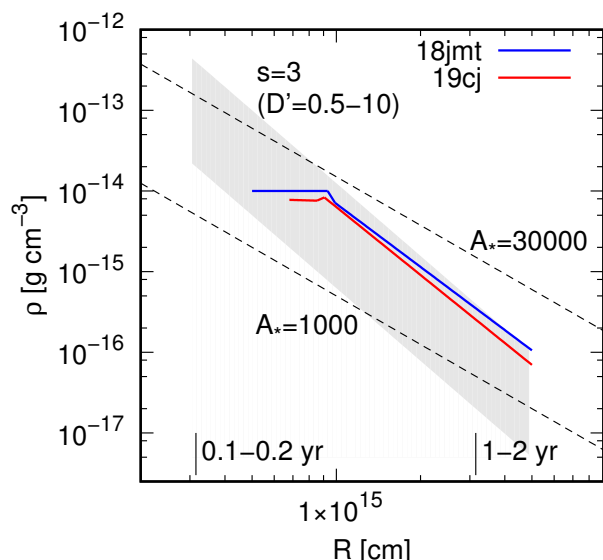
Fig. 10. The CSM radial-density distribution derived for SNe 2018jmt (blue) and 2019cj (red). The typical range found for a sample of SNe Ibn is shown by the grey-shaded area. For comparison, the CSM distribution by a steady-state mass loss is shown by the dashed lines for the CSM density parameter of $A_* = 30,000$ and $1,000$ (corresponding to $D' = 6$ and 0.2 with $s = 2.0$). On the bottom, the look-back time in the mass-loss history is indicated, assuming $v_w = 500\text{-}1,000$ km s^{-1}.

is blue-shifted by about 150 - 300 km s^{-1}). It is worth mentioning that other Balmer lines, which are prominent in Type IIn SNe, are only marginally detected in SN 2018jmt.

In the subsequent three spectra (from +18 to +56 d), the dominant feature is a blue pseudo-continuum that extends up to approximately 5600 Å. The nature of this blue pseudo-continuum has been extensively discussed by Stritzinger et al. (2012) and Smith et al. (2012). They propose that it arises from a combination of numerous narrow and intermediate-width Fe lines, similar to those observed in SN 2005ip (with a $v_{FWHM} \sim$ 150 - 200 km s^{-1}) and SN 2006jc (with a $v_{FWHM} \approx$2000 - 2500 km s^{-1}; Chugai 2009). This blend of Fe lines can explain several features observed in the spectrum of SN 2018jmt. They account for the apparent discontinuity in the continuum at around 5600 Å, the broad 'W'-shaped feature between 4600 and 5200 Å (although some He I lines may also contribute to it), and the broad bump observed between 6100 and 6600 Å.

At 18.4 days after maximum, prominent He I lines in emission are observed at λ3889, λ4388 (weak), λ4471, $\lambda\lambda$4921, 5016, λ5876 (possibly blended with the Na I doublet), λ6678, λ7065, and λ7281. These lines exhibit an emission component that largely dominates over the blue-shifted absorption. The most prominent He I emission features display a distinct double-component profile. By deconvolving the λ7065 line into Lorentzian and Gaussian components, we deduce the presence of a broader component with a FWHM velocity of $\sim$ 2800 km s^{-1}, which shows marginal evolution over time. Additionally, a narrower line with a FWHM velocity of $\sim$ 950 km s^{-1} is superimposed on the broader component. From this spectrum, there is a marginal detection of the Hα line (possibly blended with C II λ6578) and possibly even Hβ. We also identify Mg I λ5528, Ca II H&K $\lambda\lambda$3934,3969, as well as O I λ6158. We searched for the presence of lines typical of thermonuclear SNe, such as S II and Si II ions, but we were unable to securely identify them. It is likely that Fe II lines are responsible for the majority of the

broad absorption blends observed at $\lambda <$ 5600 Å. Additionally, broad bumps are detected around 7900 Å (likely attributed to Mg II $\lambda\lambda$7877,7896), 8200 Å (possibly Mg II $\lambda\lambda$8214,8235 lines), 8500 Å (due to Ca II NIR triplet), and 9200 Å (attributed to Mg II $\lambda\lambda$9218,9244 lines).

At later epochs, the emission lines become stronger, allowing for a more robust identification of the spectral features. Using our latest spectra taken at 41.5 and 56.2 days after maximum light, we accurately identify the most prominent features, as shown in Fig. 11. However, it should be noted that the S/N in these spectra is relatively low. We continue to observe the prominent He I lines, now exhibiting a FWHM velocity of $\sim$ 3200 km s^{-1}. Once again, we tentatively identify Hα and Hβ ($v_{FWHM} \sim$ 600 km s^{-1}) emission lines, although alternative identifications cannot be completely ruled out, such as C II (λ 6578) and N II (λ 4803).

5.2. Spectral sequence of SN 2019cj

The spectroscopic monitoring campaign of SN 2019cj began 4 days after its discovery and lasted for 20 days. Information regarding the spectroscopic observations can be found in Table B.2, while the sequence of available spectra for SN 2019cj is shown in Fig. 11, bottom panel.

The first spectrum, obtained 8.1 days after the explosion (i.e., 2.1 days before the maximum light), exhibits a blue continuum. By fitting a blackbody to the continuum, we infer a temperature of $T_{bb} = 16800\pm2400$ K. The most prominent emission feature is observed in the blue region of the spectrum, specifically around 4660 Å, and it displays a double-peaked profile. The redder component of the emission is most likely to be He II λ4686. On the other hand, the bluer emission is possibly attributed to either C III λ4648 or N III λ4640, or a combination of both. We note that these lines, which were also identified by Silverman et al. (2010) and Cooke et al. (2010), are commonly seen in WR winds. They are also frequently observed as "flash spectroscopy" features in very early spectra of many CC SNe (e.g., Gal-Yam et al. 2014; Bostroem et al. 2023; Bruch et al. 2023; Zhang et al. 2023; Jacobson-Galán et al. 2024b,a). A similar characteristic was also detected in the early spectra of other SNe Ibn, such as SN 2010al (Pastorello et al. 2015a) and SN 2019uo (Gangopadhyay et al. 2020). A low-contrast feature is observed around 5830-5890 Å, and it is likely due to the He I λ5876, exhibiting a weak P-Cygni profile.

Between the second and third spectra (taken 1.1 and 0.2 days before maximum light), we still observe a dominant blue continuum, with a photospheric temperature (T_{bb}) decreasing from 16700±2700 K to 14300±1900 K. The blend of lines from highly ionised elements, detected in the first spectrum at 4600−4700 Å, gradually weakens, although remaining the most prominent feature, and still displaying a double-peaked profile. In the spectrum taken at maximum light, other lines start to emerge, in particular, He I λ5876, which exhibits a very narrow P-Cygni profile. The position of the minimum of the blue-shifted absorption component suggests a velocity of the He-rich material around 740 km s^{-1}. In the fourth spectrum (+3.2 days), T_{bb} has decreased to 11900±1200 K, while the P-Cygni He I lines become progressively more prominent. From the position of the absorption minimum, we infer an expansion velocity of approximately 1200 km s^{-1}. The previously observed feature at around 4600-4700 Å has now completely vanished. Furthermore, another weak P-Cygni feature can be seen in the spectrum, specifically the He I λ6678 line. The subsequent spectrum (+5.7 days)
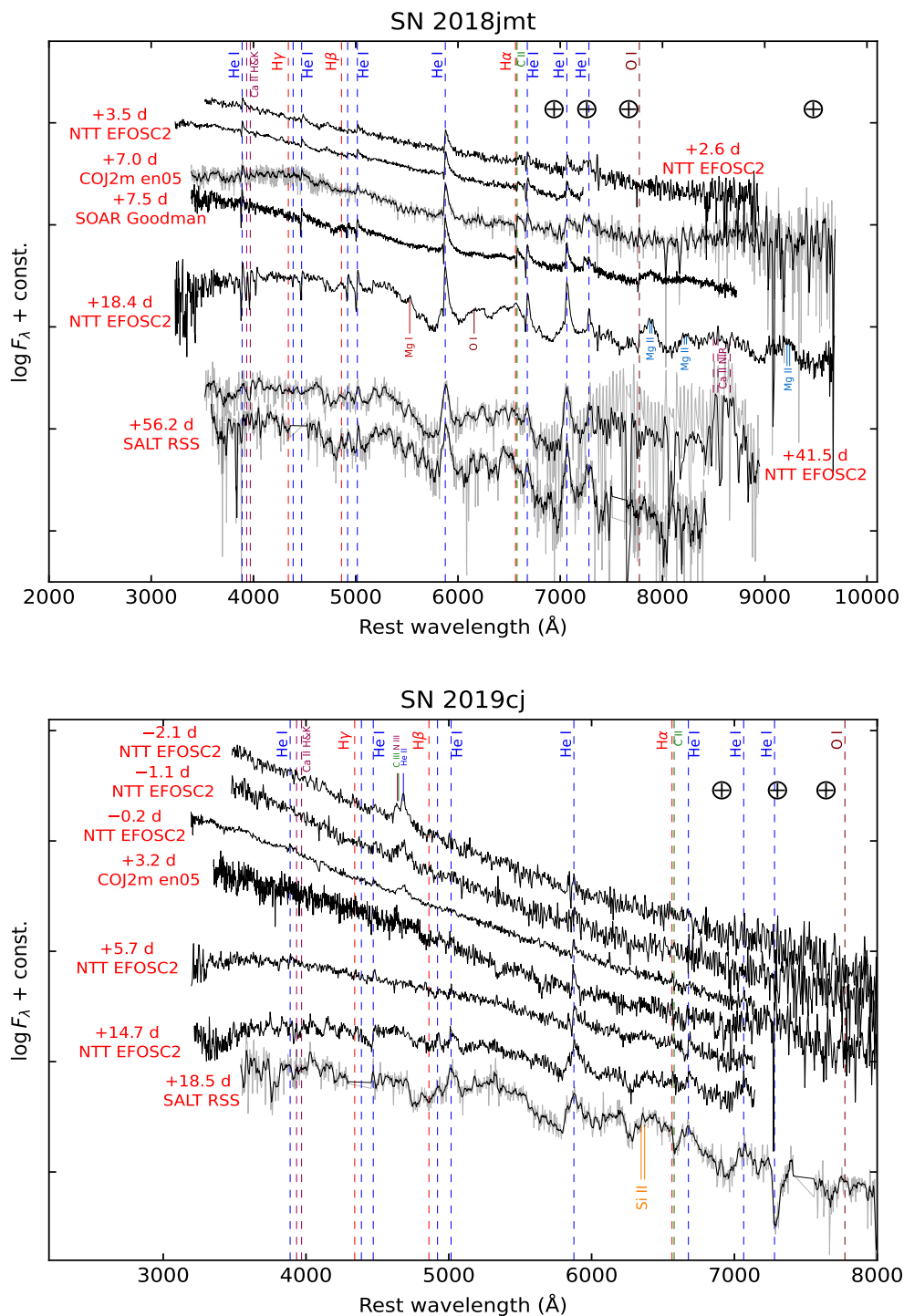
Fig. 11. Spectral sequences of SN 2018jmt (top) and SN 2019cj (bottom). The position of the principal transitions from H and He I are highlighted by the dashed vertical lines. The ⊕ symbols mark the position of the strongest telluric absorption bands. All spectra have been corrected for redshift and extinction. In some cases, spectra with lower S/N have been smoothed using a Savitzky-Golay filter (indicated by the gray line).

does not exhibit any significant changes or evolution, except a slightly redder continuum (T_{bb} = 8800±1400 K). The spectrum obtained at 14.7 days after maximum displays significant changes. The continuum has shifted towards redder colours, with a photospheric temperature of 7400±1000 K. The most prominent line observed is He I $\lambda5876$, which is mainly in emission and exhibits a FWHM of approximately 5600 km s^{-1}. Additionally, several new emission lines are detected, including He I $\lambda\lambda4921$,

5016, and $\lambda7065$. In the last spectrum taken on day 18.5, most features observed in the previous spectrum are confirmed, with a notable blue pseudo-continuum. The lines of He I $\lambda5016$, $\lambda5876$ (possibly blended with Na I D), $\lambda6678$, and $\lambda7065$ are now seen as prominent emission features. We can confidently rule out any S II features. The absorption observed around 6300 Å could potentially be attributed to Si II $\lambda6355$, while alternative identifications include Mg II $\lambda6346$ and/or [O I] $\lambda\lambda6300$, 6364.
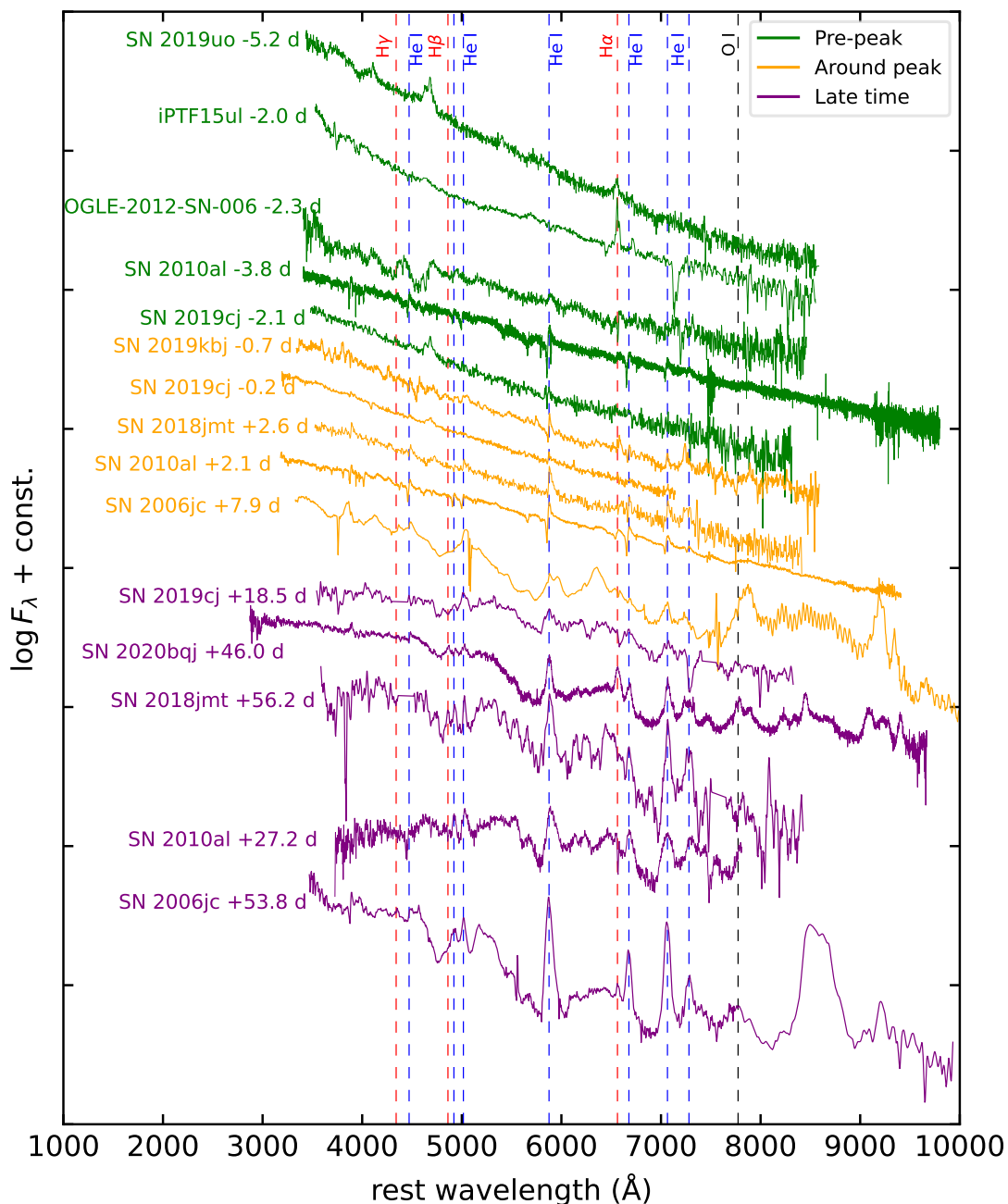
Fig. 12. Comparison of pre-peak, around peak, and late-time spectra of SN 2018jmt and SN 2019cj with those of other SNe Ibn at similar phases. The H, He I, and O I lines are marked with dashed vertical lines. All spectra have been corrected for the respective redshift and extinction. The pre-peak spectra are shown in green, those taken near the maximum light are in orange, and the post-maximum spectra are in purple. The most significant He I lines are indicated by vertical dashed blue lines, while Balmer lines are marked with red dashed lines. The O I $\lambda 7774$ line is represented by a dashed black line.

The transition of the spectral features from the 'flash' features to those of a classical Type Ibn SN might be consistent with the two-component CSM structure inferred through the LC modeling. When the shock is in the inner component (in the pre-maximum phase), with sufficiently dense materials to create the recombination lines and not yet swept up, they might create the highly-ionized emission lines as irradiated by the high-energy photons from inside. Once the shock enters into the outer component (in the post-maximum phase), the CSM density above the shock wave rapidly decreases, and thus they are not able to produce the recombination lines anymore. Note that the pre-maximum spectra to test the same prediction for SN 2018jmt are not available. However, lacking detailed spectral modeling, this picture is only speculative; this needs to be verified by future efforts in both theoretical modeling and advanced observations.

5.3. Comparison of Type Ibn SN spectra

In Fig. 12, we present a comparison of the pre-peak, around-peak, and late-time spectra of SN 2018jmt and SN 2019cj with those of other SNe Ibn at similar phases. On top of Fig. 12, an early spectrum of SN 2019cj is compared with pre-peak spec-
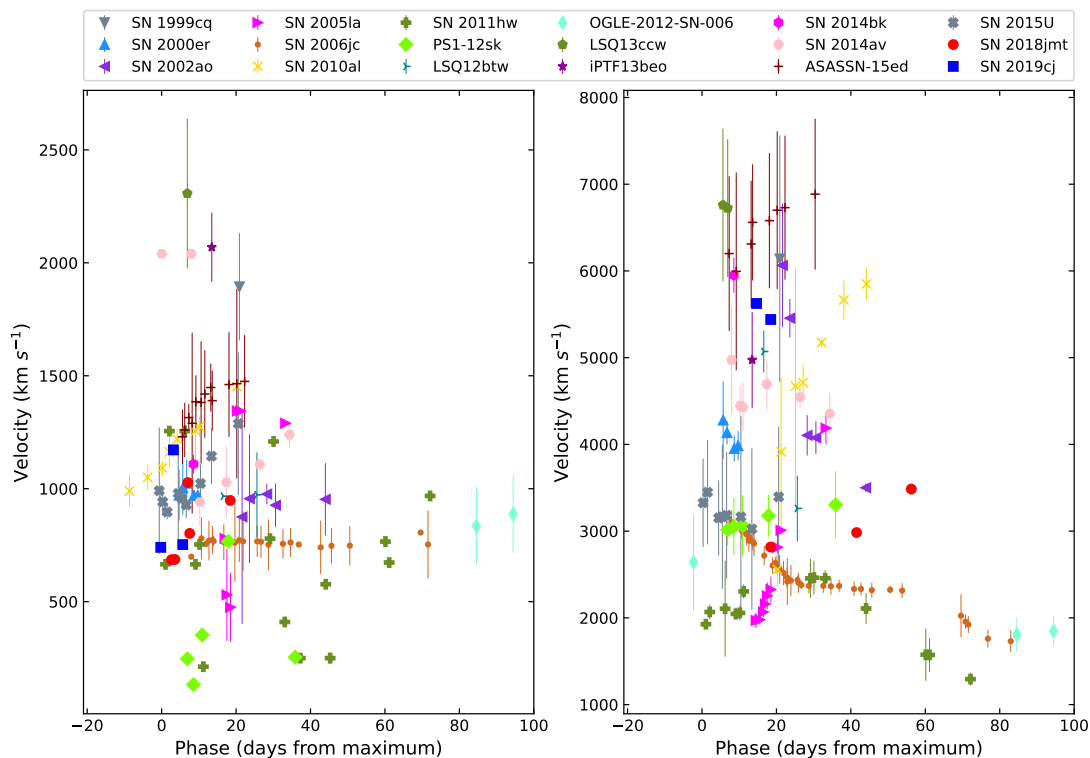
Fig. 13. Velocity evolution of the He I emission lines. In the left panel, the velocity evolution of the narrow He I line components is shown. On the right panel, the velocity of the intermediate/broad emission components is displayed. The data of comparison SNe Ibn are taken from Pastorello et al. (2016).

tra of other Type Ibn SNe, including SN 2019uo, iPTF15ul, OGLE-2012-SN-006, and SN 2010al. The pre-peak spectra of these SNe exhibit notable differences. SN 2019uo, iPTF15ul, and OGLE-2012-SN-006 display evident Hα lines, while in SN 2010al and SN 2019cj, this feature is very faint or missing. The He I λ5876 line is quite prominent in OGLE-2012-SN-006, SN 2010al, and SN 2019cj, whereas it is missing or weak in SN 2019uo and iPTF15ul. One of the strongest features visible in the early spectra SNe 2019uo and 2019cj is observed at around 4660 Å, showing a double-peak profile, likely a blend of He II and N III/C III (see Sect. 5.2). The situation is different in the OGLE-2012-SN-006 spectrum, where this line is not securely detected, but a broad absorption feature is present at a similar position, likely due to O II lines (Pastorello et al. 2015e). We remark that O II lines have never been observed before in SNe Ibn, although these lines are ubiquitously observed in the early spectra of super-luminous stripped-envelope (SE) SNe (Quimby et al. 2011).

In the middle of Fig. 12, a spectrum around the peak of SN 2018jmt and SN 2019cj is compared with spectra of SNe 2019kbj, 2010al, and 2006jc taken at similar phases. The spectra of SNe Ibn share a very similar blue continuum with narrow P-Cygni profiles of He I lines. However, there are some subtle differences. Specifically, Hα is still observable as a weak emission in SN 2019kbj and SN 2010al, while its presence is not secure in the spectra of SN 2018jmt and SN 2019cj. In this small sample, SN 2006jc is somewhat of an exception, as its spectrum shows a larger number of lines with a broader width. While the phase of SN 2006jc is measured relative to its peak time, which is relative to the presumed time of the maximum light (MJD = 54012.29, according to Maund et al. 2016), the properties of the spectrum suggest a somewhat older evolutionary phase.

At the bottom of Fig. 12, a late spectrum of SN 2018jmt and one of SN 2019cj is compared with those of SNe 2020bqj, 2010al, and 2006jc at similar phases. The spectra of the five objects exhibit a remarkable similarity in terms of the blue pseudo-continuum and the presence of prominent broader spectral lines. The wide velocity range observed in these lines can be attributed to various gas regions where they originate, such as the unperturbed CSM, shocked shells, shocked or unshocked supernova ejecta, or a combination of different emitting regions (Pastorello et al. 2016).

5.4. He I line velocity evolution

The velocity evolution of the spectral lines allows us to constrain the properties of the stellar wind and understand the nature of the emitting regions. SNe that interact with the CSM, such as Type Ibn and Type IIn events, exhibit lines with multiple-width components. These components are believed to originate from different gas regions (Chugai 1997).

In SNe Ibn, the presence of multiple components in the spectral lines indicates that the emitting material is expanding at different velocities. When a clear P-Cygni profile is identified, the velocity of the He-rich expanding material can be determined by measuring the position of the minimum point of the blue-shifted absorption. If this component is undetected, the velocity is estimated by measuring the FWHM of the strongest He I emission lines, which are obtained by deblending the full line profile using Gaussian fits. The evolution of velocities in He I emission lines is illustrated in Fig. 13.

The study of the narrowest line profiles provides insights into the velocity of the unshocked CSM hence offers key information about the mass-loss history of the progenitors of SNe Ibn in the

latest stages of its life. The temporal evolution of the velocity of the narrow He I line components is shown in the left panel of Fig. 13. In most cases, including SN 2018jmt and SN 2019cj, the narrow He I components in our spectral sample exhibit velocities of 800-1000 km s^{-1}. It is worth noting that, due to the limited spectral resolution of the spectra, the measurements for the two SNe should be considered as upper limits in some cases. However, it is worth noting that the narrowest components observed in the spectra of our Type Ibn supernova sample span a wide range of velocities. Objects such as PS1-12sk (approximately 250 km s^{-1}) and the two transitional Type Ibn/IIn SNe, SNe 2005la (about 500 km s^{-1}) and 2011hw (200-250 km s^{-1}), display the lowest velocities for the unperturbed CSM. On the other extreme, LSQ13ccw, iPTF13beo, and SN 1999cq exhibit narrow components with P-Cygni profiles having velocities of approximately 1900-2300 km s^{-1}. Such a large range of CSM velocities, as identified by Pastorello et al. (2016), suggests that Type Ibn SNe may arise from different progenitor types and/or different explosion mechanisms.

The evolution of the expansion velocities for the intermediate/broad components of the He I lines is shown in right panel of Fig. 13. These components exhibit velocities that are 4-6 times higher than those measured for the narrow components. Unlike the narrow features, the broader components of the He I lines experience a significant evolution over time. This evolution is influenced by the velocity of the ejecta and the density of the interacting material. The velocities of these broader components can provide insights into the gas interface between two shock fronts, which in turn depend on the speed of the expanding SN ejecta. An increasing velocity of the intermediate/broad He I components is observed in SN 2010al, ASASSN-15ed, SN 2018jmt, SN 2005la, and PS1-12sk. In some cases, the He I lines become narrower with time. For instance, in SN 2002ao, the width of the He I intermediate component decreases by a factor of 2 within three weeks. This trend is also observed in SNe 2014av, 2000er, 2002ao, 2019cj and 2006jc. This apparent decline in the velocity of the shocked gas regions is possibly attributed to an increased density of the CSM.

6. Summary and discussion

The high-cadence *TESS* light curve of SN 2018jmt presented by Vallely et al. (2021) reveals no evidence for a rapidly evolving shock break-out peak. The subsequent light-curve rise time to maximum light is 13.4 ± 0.3 days, slightly longer than the 10.2 days estimated in this paper for SN 2019cj (in the *T*-band and *V*-band, respectively). At maximum, SN 2018jmt and SN 2019cj exhibit a similar luminosity, reaching a peak magnitude of $M_g \sim$ -19 mag and $M_V \sim$ -19 mag, implying a very similar bolometric luminosity of about 10^{43} erg s^{-1}. The post-peak decline in the light curve of SN 2018jmt is initially steep ($\gamma_{0-15}(r) \approx$ 0.13 mag d^{-1}) and then slows down ($\gamma_{15-60}(r) \approx$ 0.04 mag d^{-1}), whereas in the case of SN 2019cj, it starts off slow ($\gamma_{0-15}(r) \approx$ 0.05 mag d^{-1}) and then becomes steep ($\gamma_{15-48}(r) \approx$ 0.09 mag d^{-1}), as reported in Table 1. This is consistent with the decline rate range of γ_{0-15}(R): 0.05 ~ 0.24 mag d^{-1} observed in the SN Ibn group (Hosseinzadeh et al. 2017).

The spectra of SN 2018jmt evolve from a distinct blue continuum in the early phases to being dominated by narrow He I lines ($v \sim$ 600 - 1000 km s^{-1}), while T_{bb} ranges from 12,000 to 9,000 K. A weak and narrow Hα line with a P-Cygni profile ($v \sim$ 150 - 300 km s^{-1}) is present, while other Balmer lines are either absent or weak. In the subsequent stages, the spectra

exhibit a blue pseudo-continuum with a narrower line superimposed on the broader component, which eventually transitions into a broad line ($v_{FWHM} \sim$ 3200 km s^{-1}). At the early stages of SN 2019cj, an intriguing feature observed in the spectra is the potential identification of flash ionisation signatures formed within a He-rich CSM. The most prominent line in the subsequent spectra of SN 2019cj was the He I line at 5876 Å, initially displaying a P−Cygni profile ($v \sim$ 740 - 1200 km s^{-1}), and later transitioning into broad features in emission ($v_{FWHM} \sim$ 5600 km s^{-1}).

The high intrinsic luminosity, the blue colours persisting for a long time, the emission-line spectra, and the fast-declining light curve without any apparent flattening to the ^{56}Co tail suggest that the observables of SNe 2018jmt and 2019cj are primarily due to ejecta−CSM interaction. In particular, as there is no spectroscopic evidence of dust formation (e.g., blue-shifted line emission peaks), the faint late-time luminosity of the two SNe (see Fig. 9) can be explained assuming that the contribution of the synthesised ^{56}Ni/^{56}Co to the light curve is very small.

From light curve modelling (see Fig. 10), we may determine the CSM configuration of SNe 2018jmt and 2019cj. The CSM distribution is constrained within a range from 5×10^{14} to 5×10^{15} cm. The inner and outer radii correspond to look-back times of approximately 0.1 to 0.2 years and 1 to 2 years, respectively, assuming a mass-loss history with $v_w = 500$ to 1000 km s^{-1}. Notably, the CSM distribution exhibits a steeper trend compared to steady-state mass loss, characterised by a power-law index of approximately s = 3. Furthermore, the derived CSM density is remarkably high for the outer components, with D' = 4.2 for SN 2018jmt and 4.4 for SN 2019cj. At a distance of approximately 5×10^{14} cm, this corresponds to $D \sim$ (4.2 and 4.4) $\times 10^{-14}$ g cm^{-1} or $A_* \sim$ 21, 000 and 22, 000; $\dot{M} \sim$ 0.21 and 0.22 $M_\odot$ yr^{-1} for $v_w = 1,000$ km s^{-1}, or $\dot{M} \sim$ 0.105 and 0.11 $M_\odot$ yr^{-1} for $v_w = 500$ km s^{-1}. These two objects exhibit an inner flat CSM component and an outer steep CSM component at a radius of approximately $(0.8 - 1) \times 10^{15}$ cm. A common feature in SNe Ibn is the possible existence of the inner flat part CSM component, as observed in SNe 2010al, 2011hw, and LSQ12btw (Maeda & Moriya 2022). Considering the time scale of the two-component CSM transition, $0.3 - 0.6$ years, it is possible that this new component corresponds to an eruptive pre-SN mass-loss event as observed in SN 2006jc (Pastorello et al. 2007). In this latter object, the outburst occurred approximately two years prior to the SN explosion.

6.1. Host environment metallicity

Pastorello et al. (2015b) conducted a characterisation study of the host galaxies of SNe Ibn, revealing that all of them were found in spiral galaxies, with the exception of PS1-12sk, which originated in the outskirts of an elliptical galaxy (Sanders et al. 2013). In order to explore the possible connection of SNe Ibn with the evolution of very massive WR stars, we study the environments of our two Type Ibn SNe. SN 2018jmt exploded within an edge-on disk galaxy, most likely a spiral galaxy, while SN 2019cj occurred in the outskirts of a late-type (Sc-type) spiral galaxy.

The oxygen abundance for the host galaxies at the SN location can be calculated using the luminosity-metallicity relation of Pilyugin et al. (2004). The oxygen abundance at the location of SN 2018jmt is approximately 8.54 dex, while for SN 2019cj, it is 8.62 dex. These values are nearly solar, assuming a Solar metallicity of 12 + log(O/H) = 8.69 dex (see e.g., Asplund

et al. 2009; von Steiger & Zurbuchen 2016; Vagnozzi 2019). Pastorello et al. (2015b) estimated an average metallicity of 12 + log(O/H) = 8.63 ± 0.42 at the SN positions for Ibn SNe. Taddia et al. (2015), using a smaller sample, found a slightly lower average oxygen abundance of 12 + log(O/H) = 8.45 ± 0.10. The discovery of SNe Ibn in environments spanning a wide range of metallicities led Pastorello et al. (2016) to suggest that metallicity has a marginal influence on the evolutionary path of the progenitors of SNe Ibn.

6.2. Progenitor and explosion scenarios

In our attempts to model the light curves of SNe 2018jmt and 2019cj, we constrained the physical parameters as follows:

- Ejecta: M_{ej} ranges between 1 $M_\odot$ to 4 $M_\odot$, and E_K is of the order of 10^{51} erg, although there is some degeneracy in the above values. Adopting an average value of $M_{ej} = 2\ M_\odot$ for the two objects, $E_K \sim 1.6 \times 10^{51}$ erg for SN 2018jmt and 1.9×10^{51} erg for SN 2019cj are required to fit the light curves. Our analysis provides lower limits for the ejecta masses as $M_{ej} > 1.6\ M_\odot$ for SN 2018jmt and $> 1.8\ M_\odot$ for SN 2019cj.
- CSM: We adopt $M_{ej} = 2\ M_\odot$ and a two-zone CSM distribution, with a flat-density inner component (s $\sim$ 0.1, $D' \sim$ 0.9) and a steeper density outer component (s $\sim$ 2.7, $D' \sim$ 4.3). Specifically, for the outer components, we obtained $(s, D') = (2.6 \pm 0.1, 4.2 \pm 0.3)$ for SN 2018jmt and $(2.8 \pm 0.1, 4.4 \pm 0.3)$ for SN 2019cj. For the inner components, we infer $(s, D') = (0.0 \pm 0.5, 1.0 \pm 0.3)$ for SN 2018jmt and $(0.1 \pm 0.5, 0.8 \pm 0.2)$ for SN 2019cj.
- ^{56}Ni production: While the light curves of the two SNe can be comfortably reproduced with a pure CSM-interaction model, without necessarily invoking a ^{56}Ni production, we could constrain an upper limit for the ejected ^{56}Ni mass from the late luminosity. Assuming ejected masses of $M_{ej} = 2\ M_\odot$ and 4 $M_\odot$, respectively, we obtained 0.15 $M_\odot$ and 0.08 $M_\odot$ as upper limits for the ^{56}Ni amounts (the above values are virtually identical for SNe 2019cj and 2018jmt).

The above CSM properties (D') are quite close to the upper limit expected for Type Ibn SNe. According to Maeda & Moriya (2022), when the mass-loss rate significantly exceeds $D' \sim 4$, the entire helium envelope is ejected. Further mass loss could then lead to the formation of a C/O−rich CSM and would result in the emergence of SNe Icn.

6.2.1. Thermonuclear SNe from He white dwarfs?

SNe 2018jmt and 2019cj exhibit a rise time of approximately 10 days, thus belonging to the well-populated sample of fast-evolving SNe Ibn. The evolutionary timescales of these SNe Ibn resemble those observed in other classes of transients. SN 2002bj (Poznanski et al. 2010), in particular, is a fast-evolving, He-rich transient that was tentatively interpreted as a helium shell detonation on a white dwarf (an example of the so-called Type .Ia SNe; see Bildsten et al. 2007). These transients are expected to be relatively faint, with peak magnitudes ranging from −15 to −18 in the *V*-band (Perets et al. 2010; Kasliwal et al. 2010; Perets et al. 2011; Fesen et al. 2017). More importantly, they exhibit a rapid evolution, typically with a rise time of 1 to 6 days, with dimmer objects usually experiencing a faster rise. The sample of Type .Ia SN candidates includes ^{56}Ni masses ranging from very small values (0.02 $M_\odot$ in the case of SN 2010X; Kasliwal et al. 2010) to ~0.2 $M_\odot$ for SN 2002bj (Kasliwal et al. 2010).

The upper limits for the ^{56}Ni mass estimated for SN 2018jmt and SN 2019cj are alone not sufficient to rule out the possibility of a Type .Ia SN interpretation.

However, the ejecta/CSM parameters estimated for SNe 2018jmt and 2019cj are inconsistent with those expected in a very low progenitor mass scenario. For instance, interpreting them as thermonuclear SNe from He white dwarfs is an improbable scenario, given the relatively high ejected masses and the overall CSM parameters. Another argument against a thermonuclear explosion of white dwarfs is the lack of the S ii spectral lines typical of SNe Ia, and also the Si II features are not securely detected. For all these reasons, we believe that the two SNe Ibn are explosions associated with much more massive, envelope-stripped stars.

6.2.2. Core-collapse SNe from moderate-mass He stars in binary systems

Important constraints on the progenitor's nature can be inferred by studying the circumstellar wind, in particular, the composition and the velocity of the CSM. SNe 2018jmt and 2019cj exhibit emission-line spectra with faint or absent H features, while the prominent lines of He I suggest wind velocities of $700 − 1000$ km s^{-1}. The broadening of the He I emission components with time suggests the presence of an intermediate-width component, and a growing intensity of the shocked region emission. The initial wind velocity is quite consistent with that expected in WR winds, although similar velocities were also observed in the Type Ibn SN 2015G (Shivvers et al. 2017), whose progenitor was proposed to be a moderate-mass He star in a binary system (Sun et al. 2020).

Ejected masses higher than $1.6 − 1.8\ M_\odot$ are consistent with those expected in canonical stripped-envelope CC SNe, or even in some giant, non-terminal eruptions of very massive stars (Karamehmetoglu et al. 2021). While a significant amount of ^{56}Ni is synthesised in a SE CC SN explosion, giant eruptions are expected to produce no ^{56}Ni. Unfortunately, for SN 2018jmt and 2019cj, we could only pose upper limits on the ^{56}Ni masses ($\leq 0.08 − 0.15\ M_\odot$), which are lower than the average ^{56}Ni production observed in canonical SE CC SNe, although similar amounts were occasionally observed in SNe Ibc (e.g. Richmond et al. 1996; Hunter et al. 2009). ^{56}Ni masses of a few $\times 10^{-3}$ $M_\odot$ were also observed in faint H-rich CC SNe (e.g. Spiro et al. 2014). However, we need to remark that the zero ^{56}Ni mass case, supportive of a non-terminal eruption, cannot be ruled out. For this reason, we can conclude that the ^{56}Ni mass constraints alone do not allow us to discriminate between CC SNe and giant eruption scenarios.

From Fig. 8, we note that most SNe Ibn cluster in a small region of the phase-space diagrams, possibly suggesting some homogeneity in the explosion scenarios and the progenitor masses, hence the involvement of moderate-mass stars rather than massive progenitors. As mentioned above, Sun et al. (2020) proposed that SNe Ibn may originate from lower-mass progenitors in interacting binary systems, and the pre-SN eruptions occasionally observed before the explosion of some Type Ibn SNe could also be triggered by binary interaction.

In brief, a plausible scenario for SNe 2018jmt and 2019cj is that they arose from the explosion of relatively massive stars producing partially stripped CC SNe. This conclusion is also supported by the inspection of the latest spectrum of SN 2018jmt (+56 d), which exhibits some similarity to the spectra of a CC SN in the transition towards the nebular phase. In fact, while the [O I] $\lambda\lambda$6300, 6364, was not securely identified, the strength-

ening of the He I $\lambda7281$ line vs. the He I $\lambda7065$ can likely be attributed to the emerging of the [Ca II] $\lambda\lambda7291$, 7324 doublet, a classical feature of CC SNe in the nebular phase.

6.2.3. The explosion of massive Wolf-Rayet stars

Another plausible scenario is that SNe 2018jmt and 2019cj mark the endpoints of the lives of higher-mass WR stars. Maeda & Moriya (2022) suggested that at least a fraction of SNe Ibn is produced by the explosion of envelope-stripped WRs with zero-age main sequence masses (M_{ZAMS}) exceeding 18 $M_\odot$. This interpretation would have some evident advantages. Invoking a massive WR progenitor would comfortably explain the eruptive pre-SN mass loss events, as well as the CSM composition and velocity of typical SNe Ibn. The observed properties of SNe 2018jmt and 2019cj are quite similar to those of classical SNe Ibn (Pastorello et al. 2016; Hosseinzadeh et al. 2017).

In this scenario, the binding energy of the helium or carbon-oxygen (C+O) core is estimated to be around 10^{51} erg (Maeda & Moriya 2022). Consequently, if the canonical explosion energy (approximately 10^{51} erg, as constrained by the light-curve analysis) is achieved during the supernova explosion following neutron star (NS) formation, a significant amount of fallback onto the NS, which may or may not lead to black hole formation, is expected. Due to this fallback, the ejection of ^{56}Ni will be minimal or nonexistent (Woosley & Weaver 1995; Zampieri et al. 1998; Maeda et al. 2007; Moriya et al. 2010). According to Valenti et al. (2009), the absence of [O I] 6300, 6364 lines in the late spectra is also in agreement with the expectations of the fallback SN scenario. During their evolution, these high-mass stars develop large cores with high luminosity. While the relationship between core nature and final evolution is yet to be fully understood (Fuller 2017; Fuller & Ro 2018), the substantial luminosity could contribute to heightened activity in the final stages just before CC, resulting in a significant increase in mass-loss rate leading up to the SN event. According to Heger et al. (2003) and Langer (2012), it is reasonable to expect that massive stars with initial masses greater than 18 $M_\odot$ lose mass through strong stellar winds also without the need for a binary companion, leaving a C+O core surrounded by a He-rich CSM.

WR stars much more massive than ~18 $M_\odot$ can also produce SN-like phenomena with properties compatible with those observed in Type Ibn SNe. Pulsational pair-instability (PPI) arises from stars with He-core masses of $30 - 64$ $M_\odot$ (Woosley et al. 2007; Woosley 2017), causing intense nuclear flashes during which the H-envelope and portions of the He core are expelled. The frequency and duration of these pulses depend on the He-core mass, with more energetic pulses resulting in longer intervals. The collisions among the ejected shells may generate luminous, interacting events with SN-like observable properties. SNe 2018jmt and 2019cj may share some of the PPI SN characteristics, such as ejecta mass, ejecta velocity, and metallicity. Karamehmetoglu et al. (2021) proposed several PPI models for a Type Ibn SN with ejecta masses up to 2.65 $M_\odot$. However, PPI SNe are expected to occur in metal-poor environments, which is not the case for SNe 2018jmt and 2019cj. The progenitors of PPI SNe are also expected to experience recurrent outbursts, as suggested by Woosley et al. (2007) and Woosley (2017).This is a potential problem for invoking the PPI SN scenario for SNe 2018jmt and 2019cj, as they both appear to be single SN-like events without previously detected eruptions. A PPI model was also proposed for SN 2006jc, which exhibited a luminous precursor two years before the alleged terminal explosion. However, subsequent investigations revealed that the progenitor

of SN 2006jc was inconsistent with an extremely massive star, thus challenging the PPI scenario. Instead, the eruptive history is more likely to be explained by more conventional binary interaction (Sun et al. 2020).

Regardless of the physical mechanisms triggering the progenitor's mass loss, studying the pre-SN eruptions, as done for SN 2006jc (Pastorello et al. 2007), is a key step to constrain the properties of the progenitor stars and the terminal explosion scenario. Indeed, pre-SN outbursts were observed for a handful of Type Ibn SNe, including SN 2011hw (Dintinjana et al. 2011), SN 2019uo (Strotjohann et al. 2021), SN 2022pda (Cai et al., in preparation), and SN 2023fyq (Brennan et al. 2024). For the latter, spectra obtained when the progenitor was quiescent and later in outburst revealed complex He I line profiles, characterised by a relatively narrow P-Cygni component, whose minimum is blue-shifted by about 1700 km s^{-1}, superposed on a very broad base (extended up to 10^4 km s^{-1}). The spectra published by Brennan et al. (2024) indicate the presence of a high-velocity progenitor's wind and a highly asymmetric CSM distribution.

Unfortunately, information on the pre-SN variability of the progenitor star is an exception in SNe Ibn, either due to the lack of archival observations of the progenitor sites, or because these SNe are simply located in distant galaxies and pre-SN outbursts are below the instrumental detection thresholds.

6.3. Concluding remarks

With the available dataset for SNe 2018jmt and 2019cj, we cannot securely constrain the mass of their progenitors and the explosion mechanism. However, several clues tend to favour a scenario according to which SNe Ibn are terminal CC SNe from massive stars. Whether the progenitors are massive WRs or lower-mass He stars in binaries is still disputed.

Maeda & Moriya (2022) argued that the progenitors of SNe Ibn are WR stars with a mass exceeding 18 $M_\odot$. The volumetric rate of SNe Ibn is approximately 1% of the CC SN population (Maeda & Moriya 2022). Although this proportion falls below the fraction of massive stars with $M_{ZAMS} \geq 18$ $M_\odot$ to those with $M_{ZAMS} \geq 8$ $M_\odot$, many of these potential SNe may have remained undetected in the optical due to a significant portion of their emission being UV radiation. Therefore, conducting high-cadence UV surveys is crucial for detecting the population of UV-emitting transients, including SNe Ibn. Future facilities, such as the Ultraviolet Transient Astronomy Satellite (ULTRA-SAT)[18] space mission (Shvartzvald et al. 2024) and the Ultraviolet Explorer (UVEX) [19] mission (Kulkarni et al. 2021) will be devoted to conducting wide-field, high-cadence surveys of the sky in the UV, which will play a critical role in studying highly energetic and fast-evolving transient objects. Additionally, there is a lack of modelling of pre-peak light curves. Hence, it is imperative to consider these limitations in future observational and theoretical endeavours. The assistance of next-generation instruments, like the Chinese Space Station Telescope (CSST)[20] and the Vera C. Rubin Observatory[21] will play a vital role in increasing the sampling frequency and refining current models of Type Ibn SNe.

---

[18] `https://www.weizmann.ac.il/ultrasat/`
[19] `https://www.uvex.caltech.edu`
[20] `http://nao.cas.cn/csst/`
[21] `https://www.lsst.org/`

References

Abdurro'uf, Accetta, K., Aerts, C., et al. 2022, ApJS, 259, 35
Anupama, G. C., Sahu, D. K., Gurugubelli, U. K., et al. 2009, MNRAS, 392, 894
Asplund, M., Grevesse, N., Sauval, A. J., & Scott, P. 2009, ARA&A, 47, 481
Becker, A. 2015, HOTPANTS: High Order Transform of PSF ANd Template Subtraction, Astrophysics Source Code Library
Bellm, E. C., Kulkarni, S. R., Graham, M. J., et al. 2019, PASP, 131, 018002
Ben-Ami, T., Arcavi, I., Newsome, M., et al. 2023, ApJ, 946, 30
Bertin, E. & Arnouts, S. 1996, A&AS, 117, 393
Bildsten, L., Shen, K. J., Weinberg, N. N., & Nelemans, G. 2007, ApJ, 662, L95
Bostroem, K. A., Pearson, J., Shrestha, M., et al. 2023, ApJ, 956, L5
Brennan, S. J., Sollerman, J., Irani, I., et al. 2024, A&A, 684, L18
Brown, T. M., Baliber, N., Bianco, F. B., et al. 2013, PASP, 125, 1031
Bruch, R. J., Gal-Yam, A., Yaron, O., et al. 2023, ApJ, 952, 119
Cai, Y. Z., Pastorello, A., Fraser, M., et al. 2018, MNRAS, 480, 3424
Cardelli, J. A., Clayton, G. C., & Mathis, J. S. 1989, ApJ, 345, 245
Castro-Segura, N., Pursiainen, M., Smith, M., & Yaron, O. 2018 Transient Name Server Classification Report, 2018-2064, 1
Chambers, K. C., Magnier, E. A., Metcalfe, N., et al. 2016, arXiv e-prints, arXiv:1612.05560
Chasovnikov, A., Lipunov, V., Kornilov, D. V., et al. 2018, Transient Name Server Discovery Report, 2018-1888, 1
Chen, T. W., Inserra, C., Fraser, M., et al. 2018, ApJ, 867, L31
Chevalier, R. A. & Fransson, C. 1994, ApJ, 420, 268
Chugai, N. N. 1997, Ap&SS, 252, 225
Chugai, N. N. 2009, MNRAS, 400, 866
Clark, P., Maguire, K., Inserra, C., et al. 2020, MNRAS, 492, 2208
Cooke, J., Ellis, R. S., Nugent, P. E., et al. 2010, The Astronomer's Telegram, 2491, 1
Crawford, S. M., Still, M., Schellart, P., et al. 2010, in Society of Photo-Optical Instrumentation Engineers (SPIE) Conference Series, Vol. 7737, Observatory Operations: Strategies, Processes, and Systems III, ed. D. R. Silva, A. B. Peck, & B. T. Soifer, 773725
Dessart, L. 2024, arXiv e-prints, arXiv:2405.04259
Di Carlo, E., Corsi, C., Arkharov, A. A., et al. 2008, ApJ, 684, 471
Dintinjana, B., Mikuz, H., Skvarc, J., et al. 2011, Central Bureau Electronic Telegrams, 2906, 1
Drout, M. R., Soderberg, A. M., Gal-Yam, A., et al. 2011, ApJ, 741, 97
Fesen, R. A., Weil, K. E., Hamilton, A. J. S., & Höflich, P. A. 2017, ApJ, 848, 130
Filippenko, A. V. 1997, ARA&A, 35, 309
Fox, O. D., Chevalier, R. A., Skrutskie, M. F., et al. 2011, ApJ, 741, 7
Fransson, C., Chevalier, R. A., Filippenko, A. V., et al. 2002, ApJ, 572, 350
Fraser, M. 2020, Royal Society Open Science, 7, 200467
Fraser, M., Stritzinger, M. D., Brennan, S. J., et al. 2021, arXiv e-prints, arXiv:2108.07278
Fuller, J. 2017, MNRAS, 470, 1642
Fuller, J. & Ro, S. 2018, MNRAS, 476, 1853
Gal-Yam, A. 2017, Observational and Physical Classification of Supernovae (Springer International Publishing), 195–237
Gal-Yam, A., Arcavi, I., Ofek, E. O., et al. 2014, Nature, 509, 471
Gal-Yam, A., Bruch, R., Schulze, S., et al. 2022, Nature, 601, 201
Gan, W.-P., Wang, S.-Q., & Liang, E.-W. 2021, ApJ, 914, 125
Gangopadhyay, A., Misra, K., Hiramatsu, D., et al. 2020, ApJ, 889, 170
Gangopadhyay, A., Misra, K., Hosseinzadeh, G., et al. 2022, ApJ, 930, 127
González-Gaitán, S., Tominaga, N., Molina, J., et al. 2015, MNRAS, 451, 2212
Gorbikov, E., Gal-Yam, A., Ofek, E. O., et al. 2014, MNRAS, 443, 671
Gorbovskoy, E. S., Lipunov, V. M., Kornilov, V. G., et al. 2013, Astronomy Reports, 57, 233
Greiner, J., Bornemann, W., Clemens, C., et al. 2008, PASP, 120, 405
Hart, K., Shappee, B. J., Hey, D., et al. 2023, arXiv e-prints, arXiv:2304.03791
Heger, A., Fryer, C. L., Woosley, S. E., Langer, N., & Hartmann, D. H. 2003, ApJ, 591, 288
Hosseinzadeh, G., Arcavi, I., Valenti, S., et al. 2017, ApJ, 836, 158
Hosseinzadeh, G., McCully, C., Zabludoff, A. I., et al. 2019, ApJ, 871, L9
Hunter, D. J., Valenti, S., Kotak, R., et al. 2009, A&A, 508, 371
Jacobson-Galán, W. V., Davis, K. W., Kilpatrick, C. D., et al. 2024a, arXiv e-prints, arXiv:2404.19006
Jacobson-Galán, W. V., Dessart, L., Davis, K. W., et al. 2024b, arXiv e-prints, arXiv:2403.02382
Jayasinghe, T., Stanek, K. Z., Kochanek, C. S., et al. 2019, MNRAS, 485, 961
Karamehmetoglu, E., Fransson, C., Sollerman, J., et al. 2021, A&A, 649, A163
Karamehmetoglu, E., Taddia, F., Sollerman, J., et al. 2017, A&A, 602, A93
Kasliwal, M. M., Kulkarni, S. R., Gal-Yam, A., et al. 2010, ApJ, 723, L98
Kochanek, C. S., Shappee, B. J., Stanek, K. Z., et al. 2017, PASP, 129, 104502
Kool, E. C., Karamehmetoglu, E., Sollerman, J., et al. 2021, A&A, 652, A136
Krühler, T., Küpcü Yoldaş, A., Greiner, J., et al. 2008, ApJ, 685, 376
Kulkarni, S. R., Harrison, F. A., Grefenstette, B. W., et al. 2021, arXiv e-prints, arXiv:2111.15608

Kuncarayakti, H., Doi, M., Aldering, G., et al. 2013, AJ, 146, 30
Landolt, A. U. 1992, AJ, 104, 340
Langer, N. 2012, ARA&A, 50, 107
Lipunov, V., Kornilov, V., Gorbovskoy, E., et al. 2012, in Astronomical Society of India Conference Series, Vol. 7, Astronomical Society of India Conference Series, 275
Loveday, J. 1996, MNRAS, 278, 1025
Lyman, J. D., Bersier, D., James, P. A., et al. 2016, MNRAS, 457, 328
Maeda, K. & Moriya, T. J. 2022, ApJ, 927, 25
Maeda, K., Tanaka, M., Nomoto, K., et al. 2007, ApJ, 666, 1069
Matheson, T., Filippenko, A. V., Chornock, R., Leonard, D. C., & Li, W. 2000, AJ, 119, 2303
Mattila, S., Meikle, W. P. S., Lundqvist, P., et al. 2008, MNRAS, 389, 141
Maund, J. R., Pastorello, A., Mattila, S., Itagaki, K., & Boles, T. 2016, ApJ, 833, 128
Meza, N. & Anderson, J. P. 2020, A&A, 641, A177
Moriya, T., Tominaga, N., Tanaka, M., et al. 2010, ApJ, 719, 1445
Moriya, T. J., Maeda, K., Taddia, F., et al. 2013, MNRAS, 435, 1520
Morokuma, T., Shibata, T., Matsumoto, E., et al. 2014, Central Bureau Electronic Telegrams, 3894, 1
Mould, J. R., Huchra, J. P., Freedman, W. L., et al. 2000, ApJ, 529, 786
Moustakas, J., Lang, D., Dey, A., et al. 2023, ApJS, 269, 3
Nagao, T., Kuncarayakti, H., Maeda, K., et al. 2023, A&A, 673, A27
Nicholls, B. & Stanek, K. Z. 2019, Transient Name Server Discovery Report, 2019-20, 1
Ouchi, R., Maeda, K., Anderson, J. P., & Sawada, R. 2021, ApJ, 922, 141
Pastorello, A., Benetti, S., Brown, P. J., et al. 2015a, MNRAS, 449, 1921
Pastorello, A., Hadjiyska, E., Rabinowitz, D., et al. 2015b, MNRAS, 449, 1954
Pastorello, A., Mattila, S., Zampieri, L., et al. 2008a, MNRAS, 389, 113
Pastorello, A., Prieto, J. L., Elias-Rosa, N., et al. 2015c, MNRAS, 453, 3649
Pastorello, A., Quimby, R. M., Smartt, S. J., et al. 2008b, MNRAS, 389, 131
Pastorello, A., Smartt, S. J., Mattila, S., et al. 2007, Nature, 447, 829
Pastorello, A., Tartaglia, L., Elias-Rosa, N., et al. 2015d, MNRAS, 454, 4293
Pastorello, A., Wang, X. F., Ciabattari, F., et al. 2016, MNRAS, 456, 853
Pastorello, A., Wyrzykowski, Ł., Valenti, S., et al. 2015e, MNRAS, 449, 1941
Pellegrino, C., Howell, D. A., Terreran, G., et al. 2022, ApJ, 938, 73
Perets, H. B., Badenes, C., Arcavi, I., Simon, J. D., & Gal-yam, A. 2011, ApJ, 730, 89
Perets, H. B., Gal-Yam, A., Mazzali, P. A., et al. 2010, Nature, 465, 322
Perley, D. A., Fremling, C., Sollerman, J., et al. 2020, ApJ, 904, 35
Perley, D. A., Sollerman, J., Schulze, S., et al. 2022, ApJ, 927, 180
Pignata, G., Rodriguez, O., Gromadzki, M., & Yaron, O. 2019, Transient Name Server Classification Report, 2019-42, 1
Pilyugin, L. S., Vílchez, J. M., & Contini, T. 2004, A&A, 425, 849
Poznanski, D., Chornock, R., Nugent, P. E., et al. 2010, Science, 327, 58
Prentice, S. J., Maguire, K., Boian, I., et al. 2020, MNRAS, 499, 1450
Pursiainen, M., Leloudas, G., Schulze, S., et al. 2023, ApJ, 959, L10
Quimby, R. M., Kulkarni, S. R., Kasliwal, M. M., et al. 2011, Nature, 474, 487
Reguitti, A., Pastorello, A., Pignata, G., et al. 2022, A&A, 662, L10
Richmond, M. W., van Dyk, S. D., Ho, W., et al. 1996, AJ, 111, 327
Ricker, G. R., Winn, J. N., Vanderspek, R., et al. 2015, Journal of Astronomical Telescopes, Instruments, and Systems, 1, 014003
Sanders, N. E., Soderberg, A. M., Foley, R. J., et al. 2013, ApJ, 769, 39
Schlafly, E. F. & Finkbeiner, D. P. 2011, ApJ, 737, 103
Schlegel, E. M. 1990, MNRAS, 244, 269
Shappee, B., Prieto, J., Stanek, K. Z., et al. 2014, in American Astronomical Society Meeting Abstracts, Vol. 223, American Astronomical Society Meeting Abstracts #223, 236.03
Shingles, L., Smith, K. W., Young, D. R., et al. 2021, Transient Name Server AstroNote, 7, 1
Shivvers, I., Zheng, W., Van Dyk, S. D., et al. 2017, MNRAS, 471, 4381
Shivvers, I., Zheng, W. K., Mauerhan, J., et al. 2016, MNRAS, 461, 3057
Shvartzvald, Y., Waxman, E., Gal-Yam, A., et al. 2024, ApJ, 964, 74
Silverman, J. M., Kleiser, I. K. W., Morton, A. J. L., & Filippenko, A. V. 2010, Central Bureau Electronic Telegrams, 2223, 1
Skrutskie, M. F., Cutri, R. M., Stiening, R., et al. 2006, AJ, 131, 1163
Smartt, S. J., Valenti, S., Fraser, M., et al. 2015, A&A, 579, A40
Smith, K. W., Smartt, S. J., Young, D. R., et al. 2020, PASP, 132, 085002
Smith, N. 2017, Interacting Supernovae: Types IIn and Ibn (Cham: Springer International Publishing), 403–429
Smith, N., Foley, R. J., & Filippenko, A. V. 2008, ApJ, 680, 568
Smith, N., Mauerhan, J. C., Silverman, J. M., et al. 2012, MNRAS, 426, 1905
Spergel, D. N., Bean, R., Doré, O., et al. 2007, ApJS, 170, 377
Spiro, S., Pastorello, A., Pumo, M. L., et al. 2014, MNRAS, 439, 2873
Stetson, P. B. 1987, PASP, 99, 191
Stritzinger, M., Taddia, F., Fransson, C., et al. 2012, ApJ, 756, 173
Strotjohann, N. L., Ofek, E. O., Gal-Yam, A., et al. 2021, ApJ, 907, 99
Sun, N.-C., Maund, J. R., Hirai, R., Crowther, P. A., & Podsiadlowski, P. 2020, MNRAS, 491, 6000
Taddia, F., Sollerman, J., Fremling, C., et al. 2015, A&A, 580, A131

Tody, D. 1986, in Proc. SPIE, Vol. 627, Instrumentation in astronomy VI, ed. D. L. Crawford, 733

Tody, D. 1993, in Astronomical Society of the Pacific Conference Series, Vol. 52, Astronomical Data Analysis Software and Systems II, ed. R. J. Hanisch, R. J. V. Brissenden, & J. Barnes, 173

Tonry, J. L., Denneau, L., Heinze, A. N., et al. 2018, PASP, 130, 064505

Vagnozzi, S. 2019, Atoms, 7, 41

Valenti, S., Pastorello, A., Cappellaro, E., et al. 2009, Nature, 459, 674

Vallely, P. J., Kochanek, C. S., Stanek, K. Z., Fausnaugh, M., & Shappee, B. J. 2021, MNRAS, 500, 5639

Vallely, P. J., Prieto, J. L., Stanek, K. Z., et al. 2018, MNRAS, 475, 2344

von Steiger, R. & Zurbuchen, T. H. 2016, ApJ, 816, 13

Wang, L., Hu, M., Wang, L., et al. 2024a, Nature Astronomy, 8, 504

Wang, Q., Goel, A., Dessart, L., et al. 2024b, MNRAS, 530, 3906

Wang, S.-Q. & Li, L. 2020, ApJ, 900, 83

Wang, X., Lin, W., Zhang, J., et al. 2021, ApJ, 917, 97

Woosley, S. E. 2017, ApJ, 836, 244

Woosley, S. E., Blinnikov, S., & Heger, A. 2007, Nature, 450, 390

Woosley, S. E. & Weaver, T. A. 1995, ApJS, 101, 181

Yaron, O. & Gal-Yam, A. 2012, PASP, 124, 668

Zampieri, L., Shapiro, S. L., & Colpi, M. 1998, ApJ, 502, L149

Zhang, J., Lin, H., Wang, X., et al. 2023, Science Bulletin, 68, 2548

1   School of Physics and Astronomy, Beijing Normal University, Beijing 100875, P.R. China

2   Department of Physics, Faculty of Arts and Sciences, Beijing Normal University, Zhuhai 519087, P.R. China

3   INAF - Osservatorio Astronomico di Padova, Vicolo dell'Osservatorio 5, 35122 Padova, Italy

4   Department of Astronomy, Kyoto University, Kitashirakawa-Oiwake-cho, Sakyo-ku, Kyoto 606-8502, Japan

5   INAF - Osservatorio Astronomico di Brera, Via E. Bianchi 46, 23807 Merate (LC), Italy

6   Yunnan Observatories, Chinese Academy of Sciences, Kunming 650216, P.R. China

7   International Centre of Supernovae, Yunnan Key Laboratory, Kunming 650216, P.R. China

8   Key Laboratory for the Structure and Evolution of Celestial Objects, Chinese Academy of Sciences, Kunming 650216, P.R. China

9   Las Cumbres Observatory, 6740 Cortona Drive, Suite 102, Goleta, CA 93117-5575, USA

10 Department of Physics, University of California, Santa Barbara, CA 93106-9530, USA

11 South African Astronomical Observatory, PO Box 9, Observatory 7935, Cape Town, South Africa

12 INAF - Osservatorio Astronomico di Roma, via Frascati 33, I-00078, Monte Porzio Catone, Italy

13 Instituto de Estudios Astrofísicos, Facultad de Ingeniería y Ciencias, Universidad Diego Portales, Av. Ejército Libertador 441, Santiago, Chile

14 Graduate Institute of Astronomy, National Central University, 300 Jhongda Road, 32001 Jhongli, Taiwan

15 Institute of Space Sciences (ICE, CSIC), Campus UAB, Carrer de Can Magrans, s/n, E-08193 Barcelona, Spain

16 Department of Particle Physics and Astrophysics, Weizmann Institute of Science, 76100 Rehovot, Israel

17 The Oskar Klein Centre, Department of Astronomy, Stockholm University, AlbaNova, SE-10691 Stockholm, Sweden

18 Astronomical Observatory, University of Warsaw, Al. Ujazdowskie 4, 00-478 Warszawa, Poland

19 Guangxi Key Laboratory for Relativistic Astrophysics, School of Physical Science and Technology, Guangxi University, Nanning 530004, P.R. China

20 Center for Astrophysics | Harvard & Smithsonian, 60 Garden Street, Cambridge, MA 02138-1516, USA

21 The NSF AI Institute for Artificial Intelligence and Fundamental Interactions, USA

22 Department of Physics, Tsinghua University, Beijing 100084, P.R. China

23 Cardiff Hub for Astrophysics Research and Technology, School of Physics & Astronomy, Cardiff University, Queens Buildings, The Parade, Cardiff, CF24 3AA, UK

24 Astrophysics Research Centre, School of Mathematics and Physics, Queen's University Belfast, Belfast BT7 1NN, UK

25 UKIRT Observatory, Institute for Astronomy, 640 N. A'ohoku Place, University Park, Hilo, Hawai'i 96720, USA

26 Instituto de Alta Investigación, Universidad de Tarapacá, Casilla 7D, Arica, Chile

27 Instituto de Astrofísica, Facultad de Ciencias Exactas, Universidad Andres Bello, Av. Fernández Concha 700, Santiago, Chile

28 Department of Physics, University of Warwick, Gibbet Hill Road, Coventry CV4 7AL, UK

29 Space Science Data Center-ASI, Via del Politecnico SNC, 00133 Roma, Italy

30 Max-Planck-Institut für Extraterrestrische Physik, Giessenbachstraße 1, 85748, Garching, Germany

31 Manipal Centre for Natural Sciences, Manipal Academy of Higher Education, Manipal - 576104, Karnataka, India

32 INAF - Osservatorio Astronomico d'Abruzzo, Via M. Maggini snc, 64100 Teramo, Italy

33 Physics and Astronomy Department, Johns Hopkins University, Baltimore, MD 21218, USA

34 Center for Astrophysics and Cosmology, University of Nova Gorica, Vipavska 11c, 5270 Ajdovščina, Slovenia

35 Institut d'Estudis Espacials de Catalunya (IEEC), 08860 Castelldefels (Barcelona), Spain

36 Millennium Institute of Astrophysics, Nuncio Monseñor Sotero Sanz 100, Of. 104, Providencia, Santiago, Chile

37 Center for Fundamental Physics, School of Mechanics and optic-electrical Physics, Anhui University of Science and Technology, Huainan, Anhui 232001, P.R. China

38 Purple Mountain Observatory, Chinese Academy of Sciences, 10 Yuan Hua Road, Nanjing, Jiangsu 210023, P.R. China

39 Institute for Frontier in Astronomy and Astrophysics, Beijing Normal University, Beijing 102206, P.R. China

40 Advanced Institute of Natural Sciences, Beijing Normal University, Zhuhai 519087, P.R. China

Our observations will be made public via the Weizmann Interactive Supernova Data Repository (WISeREP; Yaron & Gal-Yam 2012).

Appendix A: Photometric tables

Table A.1. Optical and NIR observed magnitudes of SN 2018jmt.

Date	MJD	Phase	Filter	Magnitude	Error	Instrument/Source
20181123	58445.173	-20.49	g	>17.4		ASAS-SN
20181125	58447.056	-18.60	g	>18.0		ASAS-SN
20181126	58448.252	-17.41	g	>18.4		ASAS-SN
20181129	58451.304	-14.36	g	>18.4		ASAS-SN
20181129	58451.868	-13.79	g	>18.9		ASAS-SN
20181130	58452.300	-13.36	g	>18.7		ASAS-SN
20181201	58453.297	-12.36	g	>18.9		ASAS-SN
20181201	58453.869	-11.79	g	>18.6		ASAS-SN
20181202	58454.306	-11.35	g	>18.6		ASAS-SN
20181205	58457.285	-8.38	g	18.324	0.198	ASAS-SN
20181207	58459.282	-6.38	g	18.186	0.195	ASAS-SN
20181208	58460.278	-5.38	Clear	16.5	-	MASTER
20181209	58461.113	-4.55	g	17.199	0.095	ASAS-SN
20181210	58462.251	-3.41	g	17.108	0.101	ASAS-SN
20181212	58464.300	-1.36	g	16.708	0.070	ASAS-SN
20181216	58468.135	2.47	g	17.179	0.112	ASAS-SN
20181216	58468.300	2.64	V	17.153	0.012	EFOSC
20181216	58468.971	3.31	g	17.581	0.122	ASAS-SN
20181217	58469.170	3.51	V	17.236	0.019	EFOSC
20181217	58469.302	3.64	g	17.417	0.116	ASAS-SN
20181218	58470.890	5.23	U	16.778	0.023	fa06
20181218	58470.890	5.23	B	17.514	0.010	fa06
20181218	58470.890	5.23	V	17.433	0.021	fa06
20181218	58470.905	5.24	g	17.332	0.011	fa06
20181218	58470.905	5.24	r	17.536	0.020	fa06
20181218	58470.905	5.24	i	17.660	0.020	fa06
20181219	58471.870	6.21	U	16.890	0.018	fa16
20181219	58471.870	6.21	B	17.649	0.012	fa16
20181219	58471.870	6.21	V	17.499	0.016	fa16
20181219	58471.885	6.22	g	17.595	0.016	fa16
20181219	58471.885	6.22	r	17.628	0.018	fa16
20181219	58471.885	6.22	i	17.761	0.022	fa16
20181220	58472.180	6.52	U	16.994	0.014	fa15
20181220	58472.180	6.52	B	17.670	0.005	fa15
20181220	58472.180	6.52	V	17.522	0.009	fa15
20181220	58472.195	6.53	g	17.545	0.006	fa15
20181220	58472.195	6.53	r	17.657	0.014	fa15
20181220	58472.195	6.53	i	17.834	0.020	fa15
20181222	58474.095	8.43	U	17.323	0.018	fa15
20181222	58474.095	8.43	B	17.902	0.009	fa15
20181222	58474.095	8.43	V	17.746	0.026	fa15
20181222	58474.105	8.44	g	17.778	0.011	fa15
20181222	58474.105	8.44	r	17.896	0.022	fa15
20181222	58474.105	8.44	i	17.970	0.022	fa15
20181223	58475.035	9.38	U	17.486	0.018	fa06
20181223	58475.035	9.38	B	18.086	0.010	fa06
20181223	58475.035	9.38	V	17.845	0.014	fa06
20181223	58475.055	9.39	g	17.827	0.013	fa06
20181223	58475.055	9.39	r	17.964	0.024	fa06
20181223	58475.055	9.39	i	18.001	0.024	fa06
20181223	58475.300	9.64	U	17.517	0.025	fa15
20181223	58475.300	9.64	B	18.099	0.007	fa15
20181223	58475.300	9.64	V	17.930	0.009	fa15

Table A.1 – continued from previous page

Date	MJD	Phase	Filter	Magnitude	Error	Instrument/Source
20181223	58475.315	9.65	g	17.950	0.007	fa15
20181223	58475.315	9.65	r	18.080	0.015	fa15
20181223	58475.315	9.65	i	18.121	0.018	fa15
20181225	58477.015	11.35	B	18.511	0.017	fa16
20181225	58477.015	11.35	V	18.138	0.017	fa16
20181225	58477.025	11.36	g	18.314	0.021	fa16
20181225	58477.025	11.36	r	18.345	0.035	fa16
20181225	58477.025	11.36	i	18.291	0.023	fa16
20181228	58480.093	14.43	g	18.806	0.287	ASAS-SN
20181231	58483.173	17.51	J	18.109	0.026	SOFI
20181231	58483.173	17.51	H	18.028	0.061	SOFI
20181231	58483.173	17.51	K	17.713	0.073	SOFI
20190101	58484.090	18.43	V	18.741	0.027	EFOSC
20190101	58484.280	18.62	B	19.152	0.014	fa03
20190101	58484.280	18.62	V	18.824	0.014	fa03
20190101	58484.295	18.63	g	18.981	0.009	fa03
20190101	58484.295	18.63	r	18.909	0.014	fa03
20190101	58484.295	18.63	i	18.930	0.025	fa03
20190103	58486.155	20.49	B	19.218	0.023	fa15
20190103	58486.155	20.49	V	18.912	0.029	fa15
20190103	58486.170	20.51	g	19.145	0.017	fa15
20190103	58486.170	20.51	i	19.010	0.052	fa15
20190105	58488.289	22.63	g	19.115	0.289	ASAS-SN
20190107	58490.135	24.47	B	19.484	0.013	fa15
20190107	58490.135	24.47	V	19.093	0.013	fa15
20190107	58490.155	24.49	g	19.244	0.014	fa15
20190107	58490.155	24.49	r	19.284	0.017	fa15
20190107	58490.155	24.49	i	19.299	0.018	fa15
20190111	58494.215	28.55	B	19.656	0.018	fa15
20190111	58494.215	28.55	V	19.343	0.021	fa15
20190111	58494.230	28.57	g	19.447	0.015	fa15
20190111	58494.230	28.57	r	19.484	0.026	fa15
20190111	58494.230	28.57	i	19.541	0.025	fa15
20190114	58497.615	31.95	B	19.938	0.022	fa11
20190114	58497.615	31.95	V	19.533	0.031	fa11
20190114	58497.635	31.97	g	19.715	0.023	fa11
20190114	58497.635	31.97	r	19.728	0.029	fa11
20190114	58497.635	31.97	i	19.819	0.026	fa11
20190118	58501.305	35.64	B	19.981	0.034	fa15
20190118	58501.305	35.64	V	19.639	0.031	fa15
20190118	58501.320	35.66	g	19.781	0.028	fa15
20190118	58501.320	35.66	r	19.864	0.039	fa15
20190118	58501.320	35.66	i	20.129	0.072	fa15
20190122	58505.910	40.25	B	20.239	0.057	fa14
20190122	58505.910	40.25	V	19.739	0.086	fa14
20190122	58505.925	40.26	g	20.000	0.046	fa14
20190122	58505.925	40.26	r	20.037	0.069	fa14
20190122	58505.925	40.26	i	20.193	0.099	fa14
20190124	58507.200	41.54	V	19.953	0.057	EFOSC
20190126	58509.160	43.50	J	20.081	0.145	SOFI
20190126	58509.160	43.50	H	19.295	0.276	SOFI
20190126	58509.160	43.50	K	19.204	0.184	SOFI
20190127	58510.240	44.58	U	20.050	0.062	EFOSC
20190127	58510.990	45.33	B	20.303	0.051	fa16
20190128	58511.085	45.42	B	20.327	0.046	fa15
20190128	58511.085	45.42	V	20.022	0.034	fa15
20190128	58511.105	45.44	g	20.093	0.027	fa15
20190128	58511.105	45.44	r	20.236	0.033	fa15
20190128	58511.105	45.44	i	20.747	0.056	fa15
20190202	58516.265	50.60	B	20.528	0.032	fa15
20190202	58516.265	50.60	V	20.263	0.044	fa15

Table A.1 – continued from previous page

Date	MJD	Phase	Filter	Magnitude	Error	Instrument/Source
20190202	58516.285	50.62	g	20.315	0.033	fa15
20190202	58516.285	50.62	r	20.377	0.059	fa15
20190202	58516.285	50.62	i	20.680	0.069	fa15
20190207	58521.185	55.52	B	20.704	0.073	fa03
20190207	58521.185	55.52	V	20.629	0.112	fa03
20190207	58521.200	55.54	g	20.291	0.041	fa03
20190207	58521.200	55.54	r	20.363	0.079	fa03
20190207	58521.200	55.54	i	>19.6		fa03
20190208	58522.190	56.53	U	20.447	0.072	EFOSC
20190208	58522.190	56.53	V	20.494	0.093	EFOSC
20190208	58522.200	56.54	z	13.737	1.249	EFOSC
20190214	58528.090	62.43	g	20.835	0.042	GROND
20190214	58528.090	62.43	r	20.801	0.027	GROND
20190214	58528.090	62.43	i	20.857	0.045	GROND
20190214	58528.090	62.43	z	17.171	2.236	GROND
20190214	58528.090	62.43	J	19.857	0.105	GRONDIR
20190214	58528.090	62.43	H	19.420	0.131	GRONDIR
20190214	58528.090	62.43	K	>18.4		GRONDIR
20190226	58540.207	74.55	J	20.619	0.140	SOFI
20190226	58540.207	74.55	H	19.812	0.302	SOFI
20190226	58540.207	74.55	K	19.777	0.267	SOFI
20190320	58562.147	96.49	J	20.924	0.157	SOFI
20190320	58562.147	96.49	H	20.300	0.201	SOFI
20190320	58562.147	96.49	K	19.569	0.251	SOFI

Table A.2. Optical, ATLAS and NIR observed magnitudes of SN 2019cj.

Date	MJD	Phase	Filter	Magnitude	Error	Instrument/Source
20181129	58451.517	-40.92	o	>19.8		ATLAS
20181129	58451.998	-40.44	g	>19.2		ASAS-SN
20181203	58455.123	-37.32	g	>19.5		ASAS-SN
20181205	58457.104	-35.34	g	>19.1		ASAS-SN
20181206	58458.120	-34.32	g	>19.1		ASAS-SN
20181207	58459.174	-33.27	g	>19.1		ASAS-SN
20181208	58460.065	-32.38	g	>19.3		ASAS-SN
20181212	58464.271	-28.17	g	>19.3		ASAS-SN
20181213	58465.428	-27.01	o	>18.6		ATLAS
20181215	58467.429	-25.01	o	>20.1		ATLAS
20181216	58468.083	-24.36	g	>18.9		ASAS-SN
20181217	58469.442	-23.00	o	>19.7		ATLAS
20181219	58471.093	-21.35	g	>18.6		ASAS-SN
20181219	58471.443	-21.00	o	>20.0		ATLAS
20181221	58473.434	-19.01	o	>18.7		ATLAS
20181225	58477.087	-15.35	g	>18.6		ASAS-SN
20181226	58478.065	-14.38	g	>18.9		ASAS-SN
20181227	58479.240	-13.20	g	>18.8		ASAS-SN
20181227	58479.393	-13.05	o	>20.2		ATLAS
20181229	58481.114	-11.33	g	>19.4		ASAS-SN
20181229	58481.295	-11.15	g	>18.7		ASAS-SN
20181231	58483.424	-9.02	o	19.752	0.270	ATLAS
20190101	58484.074	-8.37	g	>19.1		ASAS-SN
20190102	58485.237	-7.20	g	18.624	0.234	ASAS-SN
20190102	58485.413	-7.03	c	18.733	0.097	ATLAS
20190103	58486.262	-6.18	g	18.343	0.179	ASAS-SN
20190104	58487.215	-5.23	g	18.142	0.170	ASAS-SN
20190104	58487.404	-5.04	o	18.422	0.054	ATLAS
20190105	58488.219	-4.22	g	17.624	0.126	ASAS-SN
20190106	58489.234	-3.21	g	17.610	0.134	ASAS-SN
20190107	58490.218	-2.22	g	17.718	0.131	ASAS-SN
20190107	58490.250	-2.19	V	17.591	0.013	EFOSC

Table A.2 – continued from previous page

Date	MJD	Phase	Filter	Magnitude	Error	Instrument/Source
20190108	58491.280	-1.16	V	17.538	0.022	EFOSC
20190108	58491.293	-1.15	g	17.748	0.131	ASAS-SN
20190108	58491.380	-1.06	o	17.989	0.029	ATLAS
20190108	58491.919	-0.52	g	17.707	0.139	ASAS-SN
20190109	58492.170	-0.27	V	17.503	0.020	EFOSC
20190109	58492.279	-0.16	g	17.521	0.159	ASAS-SN
20190110	58493.207	0.77	g	17.584	0.105	ASAS-SN
20190110	58493.373	0.93	c	17.841	0.044	ATLAS
20190111	58494.005	1.56	U	16.906	0.021	fa16
20190111	58494.005	1.56	B	17.614	0.024	fa16
20190111	58494.005	1.56	V	17.573	0.040	fa16
20190111	58494.015	1.57	g	17.475	0.025	fa16
20190111	58494.015	1.57	r	17.606	0.051	fa16
20190111	58494.015	1.57	i	17.776	0.054	fa16
20190111	58494.015	1.57	z	17.932	0.125	fa16
20190111	58494.277	1.84	g	17.945	0.135	ASAS-SN
20190112	58495.219	2.78	g	17.477	0.103	ASAS-SN
20190112	58495.388	2.95	o	17.951	0.036	ATLAS
20190113	58496.920	4.48	U	17.172	0.026	fa14
20190113	58496.920	4.48	B	17.893	0.034	fa14
20190113	58496.920	4.48	V	17.701	0.024	fa14
20190113	58496.925	4.49	g	17.629	0.026	fa14
20190113	58496.925	4.49	r	17.656	0.020	fa14
20190113	58496.925	4.49	i	17.823	0.024	fa14
20190113	58496.925	4.49	z	17.931	0.057	fa14
20190114	58497.107	4.67	J	17.612	0.040	SOFI
20190114	58497.107	4.67	H	17.402	0.052	SOFI
20190114	58497.107	4.67	K	17.395	0.077	SOFI
20190114	58497.226	4.79	g	18.029	0.183	ASAS-SN
20190114	58497.364	4.92	o	17.972	0.046	ATLAS
20190114	58497.605	5.17	U	17.303	0.024	fa12
20190114	58497.605	5.17	B	17.845	0.017	fa12
20190114	58497.605	5.17	V	17.771	0.013	fa12
20190114	58497.615	5.17	g	17.707	0.011	fa12
20190114	58497.615	5.17	r	17.725	0.016	fa12
20190114	58497.615	5.17	i	17.847	0.022	fa12
20190114	58497.615	5.17	z	18.025	0.076	fa12
20190115	58498.060	5.62	V	17.718	0.022	EFOSC
20190115	58498.075	5.63	U	17.393	0.041	fa03
20190115	58498.075	5.63	B	17.904	0.024	fa03
20190115	58498.075	5.63	V	17.747	0.018	fa03
20190115	58498.085	5.64	g	17.698	0.016	fa03
20190115	58498.085	5.64	r	17.719	0.017	fa03
20190115	58498.085	5.64	i	17.843	0.019	fa03
20190115	58498.085	5.64	z	18.225	0.068	fa03
20190115	58498.143	5.70	g	17.977	0.218	ASAS-SN
20190116	58499.090	6.65	U	17.430	0.025	fa15
20190116	58499.090	6.65	B	17.982	0.022	fa15
20190116	58499.090	6.65	V	17.850	0.025	fa15
20190116	58499.098	6.66	g	18.186	0.259	ASAS-SN
20190116	58499.100	6.66	g	17.738	0.017	fa15
20190116	58499.100	6.66	r	17.811	0.020	fa15
20190116	58499.100	6.66	i	17.882	0.031	fa15
20190116	58499.100	6.66	z	18.119	0.102	fa15
20190116	58499.284	6.84	g	18.238	0.179	ASAS-SN
20190117	58500.170	7.73	U	17.609	0.073	fa03
20190117	58500.170	7.73	B	18.152	0.029	fa03
20190117	58500.170	7.73	V	17.931	0.032	fa03
20190117	58500.180	7.74	g	17.923	0.022	fa03
20190117	58500.180	7.74	r	17.832	0.018	fa03
20190117	58500.180	7.74	i	17.967	0.020	fa03

Table A.2 – continued from previous page

Date	MJD	Phase	Filter	Magnitude	Error	Instrument/Source
20190117	58500.180	7.74	z	18.121	0.059	fa03
20190117	58500.220	7.78	J	17.662	0.047	SOFI
20190117	58500.220	7.78	H	17.357	0.041	SOFI
20190117	58500.220	7.78	K	17.129	0.062	SOFI
20190118	58501.195	8.75	U	17.692	0.036	fa15
20190118	58501.195	8.75	B	18.180	0.026	fa15
20190118	58501.195	8.75	V	17.990	0.025	fa15
20190118	58501.205	8.76	g	17.906	0.019	fa15
20190118	58501.205	8.76	r	17.909	0.020	fa15
20190118	58501.205	8.76	i	18.013	0.040	fa15
20190118	58501.205	8.76	z	18.114	0.083	fa15
20190119	58502.865	10.42	U	17.744	0.064	fa14
20190119	58502.865	10.42	B	18.304	0.054	fa14
20190119	58502.865	10.42	V	18.115	0.049	fa14
20190119	58502.875	10.43	g	18.073	0.037	fa14
20190119	58502.875	10.43	r	18.011	0.038	fa14
20190119	58502.875	10.43	i	18.074	0.037	fa14
20190119	58502.875	10.43	z	18.186	0.088	fa14
20190120	58503.830	11.39	U	17.916	0.058	fa16
20190120	58503.830	11.39	B	18.391	0.043	fa16
20190120	58503.830	11.39	V	18.161	0.038	fa16
20190120	58503.835	11.39	g	18.142	0.035	fa16
20190120	58503.835	11.39	r	18.015	0.031	fa16
20190120	58503.835	11.39	i	18.095	0.037	fa16
20190120	58503.835	11.39	z	18.154	0.101	fa16
20190121	58504.560	12.12	U	18.157	0.187	fa11
20190121	58504.560	12.12	B	18.605	0.119	fa11
20190121	58504.560	12.12	V	18.342	0.089	fa11
20190121	58504.570	12.13	g	18.257	0.080	fa11
20190121	58504.570	12.13	r	18.118	0.063	fa11
20190121	58504.570	12.13	i	18.073	0.069	fa11
20190121	58504.570	12.13	z	18.148	0.160	fa11
20190124	58507.059	14.62	g	18.837	0.302	ASAS-SN
20190124	58507.150	14.71	V	18.435	0.027	EFOSC
20190124	58507.316	14.88	o	19.413	0.389	ATLAS
20190125	58508.525	16.08	U	18.849	0.044	fa12
20190125	58508.525	16.08	B	19.047	0.022	fa12
20190125	58508.525	16.08	V	18.600	0.019	fa12
20190125	58508.545	16.10	g	18.682	0.016	fa12
20190125	58508.545	16.10	r	18.479	0.020	fa12
20190125	58508.545	16.10	i	18.432	0.025	fa12
20190126	58509.071	16.63	g	18.582	0.239	ASAS-SN
20190126	58509.103	16.66	J	17.889	0.043	SOFI
20190126	58509.103	16.66	H	17.502	0.046	SOFI
20190126	58509.103	16.66	K	17.020	0.063	SOFI
20190129	58512.510	20.07	B	>18.2		fa12
20190129	58512.525	20.08	g	>17.7		fa12
20190129	58512.525	20.08	r	>17.7		fa12
20190129	58512.525	20.08	i	>17.3		fa12
20190130	58513.840	21.40	B	19.952	0.041	fa14
20190130	58513.840	21.40	V	19.225	0.039	fa14
20190130	58513.855	21.42	g	19.465	0.026	fa14
20190130	58513.855	21.42	r	19.094	0.037	fa14
20190130	58513.855	21.42	i	19.010	0.049	fa14
20190203	58517.920	25.48	B	20.430	0.067	fa14
20190204	58518.885	26.44	B	20.524	0.046	fa16
20190204	58518.885	26.44	V	19.836	0.048	fa16
20190204	58518.895	26.45	g	19.969	0.032	fa16
20190204	58518.895	26.45	r	19.513	0.028	fa16
20190204	58518.895	26.45	i	19.462	0.038	fa16
20190205	58519.330	26.89	o	19.455	0.214	ATLAS

Continued on next page

Table A.2 – continued from previous page

Date	MJD	Phase	Filter	Magnitude	Error	Instrument/Source
20190208	58522.160	29.72	U	20.843	0.075	EFOSC
20190208	58522.160	29.72	V	20.134	0.061	EFOSC
20190208	58522.160	29.72	z	19.473	0.042	EFOSC
20190209	58523.135	30.69	B	21.045	0.063	fa03
20190209	58523.135	30.69	V	20.213	0.035	fa03
20190209	58523.160	30.72	g	20.428	0.032	fa03
20190209	58523.160	30.72	r	19.995	0.028	fa03
20190209	58523.160	30.72	i	19.847	0.048	fa03
20190209	58523.323	30.88	o	19.503	0.209	ATLAS
20190216	58530.885	38.44	B	21.304	1.000	fa14
20190216	58530.885	38.44	V	21.028	0.210	fa14
20190216	58530.900	38.46	g	20.610	0.118	fa14
20190216	58530.905	38.46	r	20.307	0.100	fa14
20190216	58530.905	38.46	i	20.193	0.094	fa14
20190221	58535.115	42.67	B	>20.5		fa03
20190221	58535.115	42.67	V	21.095	0.230	fa03
20190221	58535.140	42.70	g	>20.7		fa03
20190221	58535.140	42.70	r	20.942	0.187	fa03
20190221	58535.140	42.70	i	20.832	0.205	fa03
20190226	58540.130	47.69	J	19.460	0.070	SOFI
20190226	58540.130	47.69	H	18.399	0.059	SOFI
20190226	58540.130	47.69	K	17.586	0.080	SOFI
20190301	58543.276	50.84	o	20.104	0.403	ATLAS
20190308	58550.120	57.68	U	>22.3		EFOSC
20190308	58550.120	57.68	B	22.972	0.128	EFOSC
20190308	58550.120	57.68	V	22.124	0.068	EFOSC
20190308	58550.140	57.70	g	22.276	0.114	EFOSC
20190308	58550.140	57.70	r	21.776	0.063	EFOSC
20190308	58550.140	57.70	i	21.454	0.062	EFOSC
20190308	58550.140	57.70	z	21.205	0.100	EFOSC
20190309	58551.130	58.69	V	>20.5		EFOSC
20190320	58562.030	69.59	J	20.886	0.111	SOFI
20190320	58562.030	69.59	H	19.544	0.098	SOFI
20190320	58562.030	69.59	K	18.365	0.079	SOFI

Appendix B: Spectroscopic tables

Table B.1. Log of spectroscopic observations of SN 2018jmt.

Date	MJD	Phase[a] (days)	Telescope+Instrument	Grism/Grating+Slit	Spectral range (Å)	Resolution (Å)	Exp. time (s)
20181216	58468.3	+2.6	NTT+EFOSC2	gr13+1.0"	3640-9230	21	300
20181217	58469.2	+3.5	NTT+EFOSC2	gr11+1.0"	3340-7460	16	1500
20181220	58472.7	+7.0	COJ 2m+en05	red/blu+2.0"	3150-10870	18	2700
20181221	58473.2	+7.5	SOAR+Goodman	400 l/mm+1.0"	3390-8720	6	900
20190101	58484.1	+18.4	NTT+EFOSC2	gr11/gr16+1.0"	3340-9990	16	2700/2700
20190124	58507.2	+41.5	NTT+EFOSC2	gr13+1.0"	3640-9240	21	2700
20190207	58521.9	+56.2	SALT+RSS	PG0300+1.5"	3590-8430	19	1800

[a]Phases are relative to *g*-band maximum light (MJD = 58465.66 ± 1.20; 2018-12-13) in observer frame.

Table B.2. Log of spectroscopic observations of SN 2019cj.

Date	MJD	Phase[a] (days)	Telescope+Instrument	Grism/Grating+Slit	Spectral range (Å)	Resolution (Å)	Exp. time (s)
20190107	58490.3	−2.1	NTT+EFOSC2	gr13+1.0"	3640-9230	21	600
20190108	58491.3	−1.1	NTT+EFOSC2	gr13+1.0"	3630-9230	21	600
20190109	58492.2	−0.2	NTT+EFOSC2	gr11+1.0"	3340-7460	16	2400
20190112	58495.6	+3.2	COJ 2m+en05	red/blu+2.0"	3150-10870	18	2700
20190115	58498.1	+5.7	NTT+EFOSC2	gr11+1.0"	3340-7460	16	2700
20190124	58507.1	+14.7	NTT+EFOSC2	gr11+1.0"	3340-7460	16	2x2700
20190127	58510.9	+18.5	SALT+RSS	PG0300+1.5"	3540-8330	19	1200

[a]Phases are relative to *V*-band maximum light (MJD = 58492.44 ± 0.23; 2019-01-09) in observer frame.

Appendix C: Acknowledgements